npj | computational materials

Article

Published in partnership with the Shanghai Institute of Ceramics of the Chinese Academy of Sciences

https://doi.org/10.1038/s41524-026-02034-9

Impact of higher-order exchange on the lifetime of skyrmions and antiskyrmions

Check for updates

Hendrik Schrautzer[1,6], Moritz A. Goerzen[2,3,6], Bjarne Beyer[3], Soumyajyoti Haldar[3], Pavel F. Bessarab[1,4] & Stefan Heinze[3,5] ✉

Reliable control of skyrmion lifetime is essential for realizing spintronic devices, yet the role of higher-order exchange—which can lead to skyrmion stabilization—remains largely unexplored. Here we calculate lifetimes of isolated skyrmions and antiskyrmions at transition-metal interfaces based on an atomistic spin model that includes all fourth-order exchange terms. Within harmonic transition-state theory, we evaluate both energetic and entropic contributions and find substantially enhanced lifetimes when higher-order exchange is included. The four-spin four-site interaction raises the energy barrier and lowers the curvature of the energy landscape at the collapse saddle point, increasing the pre-exponential factor. We show that skyrmions and antiskyrmions can remain thermally stable even without Dzyaloshinskii-Moriya interaction (DMI), and that tuning the four-spin term by a small amount modulates the prefactor over orders of magnitude. Our results identify higher-order exchange as a promising route to stabilize topological magnetic textures—in particular in systems lacking DMI—and to engineer their thermally activated decay.

Magnetic skyrmions[1] and antiskyrmions[2] are nanoscale, topologically non-trivial magnetic textures[3] that have garnered intense interest for their potential use in future spintronic technologies. Their small size, metastability, and efficient current-driven motion[4–8] make them attractive candidates for information storage[9], logic devices, and neuromorphic computing architectures[10–12]. These magnetic textures have been observed in various systems, including non-centrosymmetric bulk magnets[13,14], ultrathin transition-metal films[15–18], multilayers[19–21], and two-dimensional (2D) van der Waals magnets[22–31]. A key mechanism enabling their stabilization is the Dzyaloshinskii-Moriya interaction (DMI)[32,33], which emerges from spin-orbit coupling in systems with broken inversion symmetry such as surfaces[34]. In addition to DMI, frustrated Heisenberg exchange interactions—arising from competing ferromagnetic and antiferromagnetic couplings beyond nearest neighbors—have been shown to stabilize isolated skyrmions[35–39] and antiskyrmions[40] even in the absence of DMI.

Recently, higher-order exchange interactions (HOI) have come into focus as another interaction influencing skyrmion stability[15,30,31,41]. These exchange interactions, which couple more than two spins, can affect the magnetic ground-state of the system[42]. They can be important for magnetic insulators[43,44] but also for itinerant magnets[42,45,46] and can lead to complex spin structures as observed experimentally[15,47–51]. Extending the pairwise Heisenberg model within perturbation theory[52–54] gives rise to higher-order energy contributions. In this work, we focus on the fourth-order HOI term:

$$E_{4-\mathrm{spin}} = -\sum_{ijkl} C_{ijkl}(\mathbf{m}_i \cdot \mathbf{m}_j)(\mathbf{m}_k \cdot \mathbf{m}_l)\,, \tag{1}$$

including up to four different magnetic moments $\mathbf{m}_i$ (4-spin) of the system. However, if $i = k$ and $j = l$, effectively only two lattice sites (2-site) are contributing to the so called biquadratic or 4-spin-2-site interaction. Similar 4-spin-3-site and 4-spin-4-site terms have been discussed[54]. In this work these are referred to as the biquadratic, the 3-site and the 4-site HOI terms. Note, that in 6th order terms such as the bicubic interaction arise, however, their contribution is expected to be even smaller than the 4th order terms considered here due to the perturbative expansion[54].

A critical challenge in information technologies based on magnetic textures is ensuring the stability of these nanoscale bits against thermal fluctuations and thus maximizing their lifetime τ given by the Arrhenius law[55–57]:

$$\tau^{-1} = \nu_0 \mathrm{e}^{-\beta \Delta E}\,, \tag{2}$$

where $\beta = 1/(k_B T)$ with the temperature T. This does not only include maximizing the corresponding energy barrier ΔE. It has been shown that

[1]Science Institute and Faculty of Physical Sciences, University of Iceland, VR-III, 107, Reykjavík, Iceland. [2]CEMES, Université de Toulouse, CNRS, 29 rue Jeanne Marvig, F-31055 Toulouse, France. [3]Institut für Theoretische Physik und Astrophysik, Christian-Albrechts-Universität zu Kiel, D-24098 Kiel, Germany. [4]Department of Physics and Electrical Engineering, Linnaeus University, SE-39231 Kalmar, Sweden. [5]Kiel Nano, Surface, and Interface Science (KiNSIS), University of Kiel, Kiel, Germany. [6]These authors contributed equally: Hendrik Schrautzer, Moritz A. Goerzen. ✉e-mail: heinze@physik.uni-kiel.de

entropic and dynamic contributions—incorporated in the pre-exponential factor ν_0—can significantly affect the lifetime, leading to differences of several orders of magnitude even for systems with similar energy barriers[55,58–60].

The role of HOI in stabilizing skyrmions and antiskyrmions has only recently been appreciated. In particular, it has been demonstrated that the 4-site interaction can significantly alter the energy landscape enhancing the energy barrier of topological spin structures[41]. However, despite the importance of the entropic and dynamic contributions to lifetimes of magnetic textures, the effect of HOI on the pre-exponential factor—essential to quantify the stability of metastable spin states via their lifetime—has not been investigated yet.

In this work, we present the development of a general computational framework for lifetime calculations of topological spin states based on transition-state theory including higher-order exchange interactions and we use it to study lifetimes of skyrmions and antiskyrmions in ultrathin films. An efficient implementation of HOI enables us to investigate how it modifies the curvature of the energy landscape and thereby affects entropic contributions to the stability of magnetic textures. We apply our approach to study topological spin states in the famous ultrathin film system Pd/Fe/Ir(111), in which isolated skyrmions have been experimentally first observed[16,18,58], and the related system Pd/Fe/Rh(111), in which nanoscale skyrmions have been predicted based on first-principles calculations[61].

Using harmonic transition-state theory and an atomistic spin model parameterized via density functional theory (DFT), we quantify the impact of HOI on the lifetimes of isolated skyrmions and antiskyrmions. We show that the pre-exponential factor in the Arrhenius law can be modified by orders of magnitude for small changes of the 4-site 4-spin interaction within the range of typical values. Our findings highlight the potential role of HOI in determining the thermal robustness of topological spin textures and provide key insights for designing stable, nanoscale magnetic bits for device applications. This is especially interesting in light of the advent of defect-free 2D van der Waals magnets, which often exhibit inversion symmetry in their structure and therefore lack DMI but may exhibit significant HOI.

Results

Atomistic spin simulations

We investigate the stability of skyrmions (Fig. 1a) and antiskyrmions (inset of Fig. 1d) in fcc-Pd/Fe/Ir(111) and fcc-Pd/Fe/Rh(111) using an atomistic spin model parameterized via DFT calculations (see Supplementary Note 1 and Supplementary Tables 1 and 2). Note, that fcc indicates the stacking order of the Pd overlayer. In this spin model, the magnetic moments are represented as classical unit vectors $\mathbf{m}_i$ located on each site i of a 2D hexagonal lattice. The total energy of a magnetic configuration is given by the Hamiltonian

$$\begin{aligned} H = &-\sum_{ij} J_{ij}(\mathbf{m}_i \cdot \mathbf{m}_j) - \sum_{ij} \mathbf{D}_{ij} \cdot (\mathbf{m}_i \times \mathbf{m}_j) - K_u \sum_i (\mathbf{m}_i \cdot \hat{\mathbf{e}}_z)^2 - \mu \sum_i \mathbf{m}_i \cdot \mathbf{B}_{\text{ext}} - \sum_{ij} B_{ij}(\mathbf{m}_i \cdot \mathbf{m}_j)^2 \\ &-2\sum_{ijk} Y_{ijk}(\mathbf{m}_i \cdot \mathbf{m}_j)(\mathbf{m}_i \cdot \mathbf{m}_k) - \sum_{ijkl} K_{ijkl}[(\mathbf{m}_i \cdot \mathbf{m}_j)(\mathbf{m}_k \cdot \mathbf{m}_l) + (\mathbf{m}_i \cdot \mathbf{m}_l)(\mathbf{m}_j \cdot \mathbf{m}_k) - (\mathbf{m}_i \cdot \mathbf{m}_k)(\mathbf{m}_j \cdot \mathbf{m}_l)] \end{aligned} \tag{3}$$

including Heisenberg exchange, DMI, uniaxial magnetic anisotropy, Zeeman interaction as well as biquadratic, 3-site and 4-site HOI. The interaction strengths are given by J_{ij}, $\mathbf{D}_{ij}$, K_u, $\mathbf{B}_{\text{ext}}$, B_{ij}, Y_{ijk} and K_{ijkl} respectively, and μ is the size of the magnetic moment. The vector $\mathbf{D}_{ij}$ is aligned perpendicular to the connection line of the sites i and j within the plane of the magnetic film. Together with the isotropic J_{ij} the shell resolved interaction strengths have been included for up to 11 shells of neighbors. The magnetic anisotropy is treated in uniaxial approximation with the easy axis perpendicular to the film surface ($\hat{\mathbf{e}}_z$). The external magnetic field is denoted by the component perpendicular to the film surface $\mathbf{B}_{\text{ext}} = B_\perp \hat{\mathbf{e}}_z$.

The summation of the HOI (Eq. (1)) covers double counting of indices i, j, k, l, respectively leading to three distinguished terms—the biquadratic, 3-site and 4-site exchange—restricted to shortest distances between magnetic moments on the hexagonal lattice, which is why we refer to the constants as B_1, Y_1, K_1 in the following, i.e. using the same notation as in ref. 41. Note, the magnetic field is always denoted by $B_\perp$ and can thus not be confused with the biquadratic exchange interaction parameter. For a plaquette of four magnetic moments $\mathbf{m}_i$, $\mathbf{m}_j$, $\mathbf{m}_k$, $\mathbf{m}_l$ these interactions are illustrated in Fig. 1b. Here, a straight line between two magnetic moments $\mathbf{m}_i$ and $\mathbf{m}_j$ symbolizes a direct dot-product $\mathbf{m}_i \cdot \mathbf{m}_j$, while a curved connection between two of such pairs represents a product of these pairs. See for example the top sketch for the 4-site HOI in Fig. 1b representing the term $(\mathbf{m}_i \cdot \mathbf{m}_j)(\mathbf{m}_l \cdot \mathbf{m}_k)$ and refer also to ref. 54. General fourth-order HOI (Eq. (1)) include up to four different atomic sites i,j,k,l. Thus, any specific HOI term can be uniquely identified through an array of six distances between the four sites:

$$d = [d_{ij}, d_{ik}, d_{il}, d_{jk}, d_{jl}, d_{kl}], \tag{4}$$

where the distances are encoded in units of the n-th nearest neighbor distance. The unique identifier of the 4-site HOI term is for example given by d = [1, 1, 1, 1, 2, 1] meaning that all sites are in nearest neighbor distance to each other except the sites j and l, which are in second nearest neighbor distance (cf. Fig. 1b). We implemented an efficient and general preprocessing routine automatically finding the contributing sites for a given HOI identifier (see "Methods"). The identifiers for the biquadratic, 3-site and 4-site HOI discussed in this work contain mostly nearest neighbor distances. However, the implementations are valid for any combination and distance of four magnetic moments and apply to any lattice model, even three-dimensional ones[62].

To quantify the role of HOI, we compare two models previously used in ref. 41: one including HOI and one neglecting HOI. The interaction parameters for the latter model were obtained by DFT total energy calculations conducted in ref. 63 for the ultrathin film system fcc-Pd/Fe/Ir(111) and in ref. 61 for fcc-Pd/Fe/Rh(111). The HOI parameters (B_1, Y_1, K_1) were calculated in ref. 41. Note, that the inclusion of HOI modifies the first three Heisenberg exchange parameters J_1, J_2 and J_3 (see Supplementary Table 1).

Above the critical magnetic field, B_C, the ferromagnetic (FM) alignment of magnetic moments corresponds to the ground state of the system. For fcc-Pd/Fe/Ir(111) these values are B_C = 2.75 T[41] for the model considering HOI explicitly and B_C = 3.17 T[37] for the model neglecting HOI (see Supplementary Note 2 for values of fcc-Pd/Fe/Rh(111)). We focus on the field regime $B_\perp \geq B_C$, where isolated skyrmions and antiskyrmions are metastable with respect to the FM state. Such a skyrmion (antiskyrmion) at a field of $B_\perp - B_C$ = 3.95 T is visualized in Fig. 1a (inset of Fig. 1d). Note, that the critical field values are smaller if HOI are included, which follows from the fact that the skyrmion lattice phase reduces to a narrower range of magnetic fields if HOI are included compared to the model without HOI as reported in ref. 41.

Higher order exchange interactions in lifetime calculations

Harmonic transition-state theory (HTST) provides a framework for definite calculations of average lifetime (Eq. (2)) of meta-stable magnetic configurations subject to thermal fluctuations. The Hamiltonian given in Eq. (3) defines the material-specific energy surface for magnetic textures—such as skyrmions, antiskyrmions, and the FM state—and allows for the

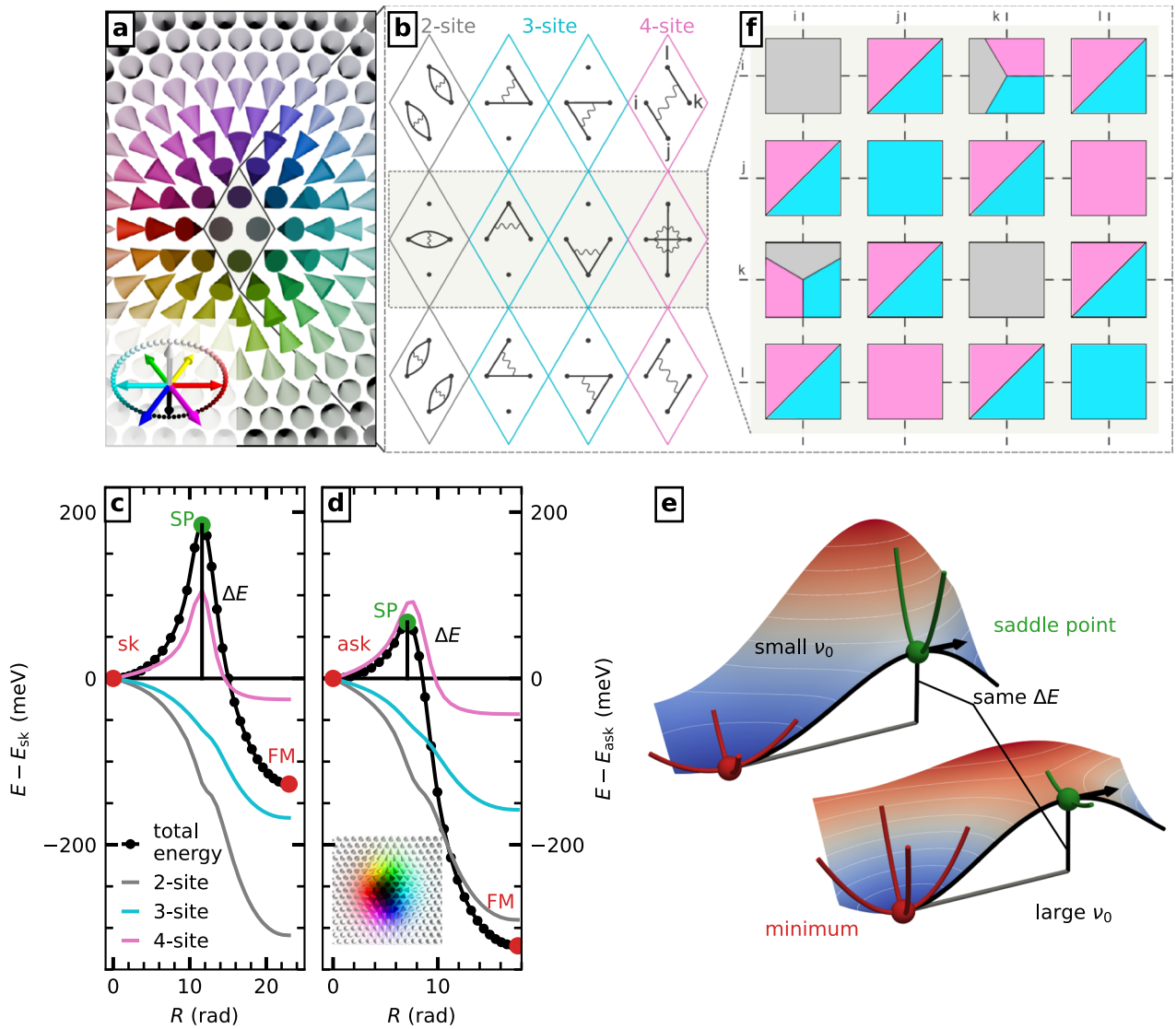


Fig. 1 | Higher-order exchange interactions and harmonic transition state theory. **a** Meta-stable skyrmion at $B_\perp - B_C = 3.95$ T in fcc-Pd/Fe/Ir(111) including higher-order exchange interactions (HOI). The color-code for the orientation of magnetic moments used in this work is shown in the lower-left corner. **b** The interactions of magnetic moments due to the biquadratic (2-site, gray), the 3-site (cyan) and the 4-site (pink) HOI are schematically depicted by straight lines (products $\mathbf{m}_i \cdot \mathbf{m}_j$) and curved lines (combinations of products) (see Eq. (3)). **c, d** Total energy including all terms in Eq. (3) (black) and HOI energy contributions (gray, cyan, pink) to the total energy as a function of the geodesic distance R along the minimum energy path (MEP) of a skyrmion (**c**) and antiskyrmion annihilation (**d**) at $B_\perp - B_C = 3.95$ T. The minima (saddle points (SPs)) are visualized by red (green) circles and the energy barrier is depicted by a vertical black line. **e** Schematic two-dimensional energy landscapes with low curvature at the minimum (red) and large curvature at the SP (green) in the upper left corner and vice versa in the lower right corner. **f** Schematic adjacency pattern for a sub-matrix of the matrix of second-order derivatives for four magnetic moments ($\mathbf{m}_i$, $\mathbf{m}_j$, $\mathbf{m}_k$, $\mathbf{m}_l$) in nearest neighbor distance of each other. For the mid row of panel **b** chosen as an example, each block is colored according to the specific HOI term contributing to its values.

computation of minimum energy paths (MEP) between them. Such a path exhibits a first-order saddle point (SP), which is the configuration with the highest energy along the MEP and yields the energy barrier for a particular transition:

$$\Delta E = E_{\mathrm{SP}} - E_{\mathrm{min}} \tag{5}$$

such as the annihilation of a skyrmion or antiskyrmion into the FM state. Figure 1c (Fig. 1d) shows the total energy—composed of all terms of Eq. (3)—along the MEP of the skyrmion (antiskyrmion) annihilation at $B_\perp - B_C =$ 3.95 T when explicitly considering HOI. The contribution of the biquadratic, 3-site and 4-site HOI to the total energy along the MEP is also shown in Fig. 1c, d. It can be seen that the 4-site HOI term plays a prominent role in increasing the barrier for both skyrmions and antiskyrmions.

Until now, studies on the role of HOI in the meta-stability of skyrmions and antiskyrmions have focused on their effect on the energy barrier alone[41,64] while neglecting entropic stabilization or destabilization effects included in the pre-exponential factor of the Arrhenius law (Eq. (2)). This term reads[55–57,65]:

$$\nu_0 = \frac{\lambda}{\sqrt{2\pi\beta}} e^{\Delta\mathcal{S}/k_B}, \tag{6}$$

where λ describes the dynamical contribution[56], and $\Delta\mathcal{S} = \mathcal{S}^{SP} - \mathcal{S}^{\mathrm{min}}$ is the relevant entropy difference between the transition state and the minimum. The $2N$ degrees of freedom of the system with N magnetic moments are treated within harmonic approximation except the unstable mode at the SP and the contribution of possible

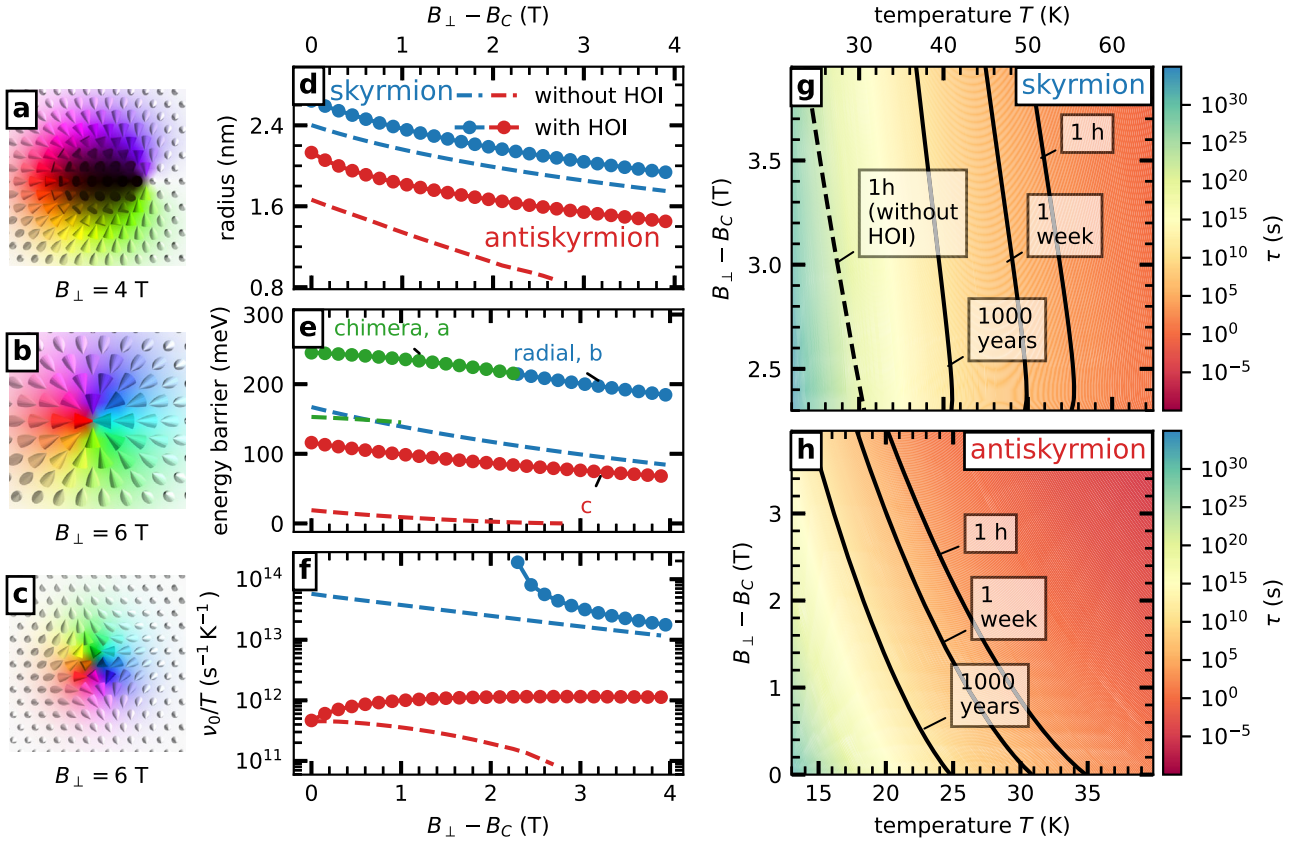


Fig. 2 | Effect of higher-order exchange interactions on skyrmion and antiskyrmion lifetime. Saddle point configuration for the collapse of the isolated skyrmion in fcc-Pd/Fe/Ir(111) including HOI at $B_\perp - B_C = 1.25$ T (**a**) and $B_\perp - B_C = 3.25$ T (**b**) and antiskyrmion at $B_\perp - B_C = 3.25$ T (**c**). **d** Radius of skyrmions (blue) and antiskyrmions (red) in fcc-Pd/Fe/Ir(111) with (solid lines and circles) and without (dashed line) explicitly considering HOI as a function of the magnetic field. The magnetic field is given relative to the field B_C for the onset of the field polarized phase for the respective energy model. **e** Energy barriers associated with the skyrmion and antiskyrmion collapse as a function of the magnetic field with and without (see refs. 41,55) explicitly considering HOI. The field regime where the Chimera collapse of the skyrmion is favoured is colored in green. **f** Pre-exponential factor ν_0 in units of temperature T plotted over $B_\perp - B_C$ for skyrmions (blue) in the regime of the radial collapse and antiskyrmions (red) for the energy model considering HOI (circles) and not explicitly taking HOI into account (dashed lines) **g** Mean lifetime τ (see colorbar) for different magnetic fields and different temperatures for the regime of radial skyrmion collapse. As a reference, the contour line for a lifetime of 1 h for skyrmions without considering HOI explicitly is also given (see ref. 55). **h** Mean lifetime of antiskyrmions taking HOI into account.

zero modes:

$$\frac{\Delta\mathcal{S}}{k_B} = \ln\left[\frac{V^{\mathrm{SP}}}{V^{\min}}\left(\frac{2\pi}{\beta}\right)^{\frac{\Delta Z}{2}}\frac{\prod_{k=1+Z^{\min}}^{2N}\sqrt{\epsilon_k^{\min}}}{\prod_{k=2+Z^{\mathrm{SP}}}^{2N}\sqrt{\epsilon_k^{\mathrm{SP}}}}\right], \tag{7}$$

where $\epsilon_k^{\min/\mathrm{SP}}$ are the eigenvalues of the Hessian of the energy reflecting the curvature of the energy surface at the critical points. An unequal number of zero modes at the minimum ($Z^{\min}$) and the SP (Z^{SP}), with volumes $V^{\min}$ and V^{SP}, yields an explicit temperature dependence with $\Delta Z = Z^{\min} - Z^{\mathrm{SP}} - 1$ for the pre-exponential factor of skyrmions and antiskyrmions (see "Methods"). Note, that the true entropy difference $\Delta\mathcal{S}'$, which arises from free energy $\mathcal{F}$ of a canonical ensemble by $\mathcal{S}' = -\partial\mathcal{F}/\partial T$, relates to the numerically relevant entropy by $\Delta\mathcal{S}' = \Delta\mathcal{S} + k_B\Delta Z/2$.

The effect of the curvatures $\epsilon_k^{\min/\mathrm{SP}}$ on the lifetime of a metastable state is schematically illustrated in Fig. 1d, where two-dimensional energy landscapes are shown with identical energy differences between a minimum and an SP, but different shape of the energy surface around them. A flat minimum combined with a sharply curved energy landscape at the SP corresponds to a large entropy barrier and yields a small ν_0, leading to a longer lifetime in such a situation. Conversely, a sharply curved energy landscape at the minimum and a less curved energy landscape at the SP increase ν_0, reducing the lifetime. Despite its importance, the influence of HOI on the curvature of the energy landscape—and thus on entropy—has not yet been systematically explored.

Similar to bilinear exchange being mediated by isotropic tensors $\underline{J}_{ij} \in \mathbb{R}^{3\times3}$ the HOI in Eq. (1) can be expressed by isotropic tensors of fourth order $\underline{C}_{ijkl} \in \mathbb{R}^{3\times3\times3\times3}$, which correspond to an interaction between lattice sites with indices i, j, k, l. Due to the multi-linearity of HOI the calculation of the second-order derivatives with respect to the components of the magnetic moments comes down to sums of quadratic forms of $\underline{C}_{ijkl}$ (see "Methods"). Figure 1f schematically shows a part of the matrix of second-order derivatives associated with the four sites i, j, k and l depicted in Fig. 1b. Each block in Fig. 1f corresponds to a (3 × 3)-block for the derivatives $\nabla_{ij}E_{4\text{-spin}}$ with respect to the m_x, m_y and m_z-components of the magnetic moments, respectively. The block colors indicate the contributing HOI terms in Fig. 1b. Note, that only the contributions from the interactions presented in the mid row of Fig. 1b are shown, which already yields a complex pattern of contributions to the displayed sub-matrix. In comparison, bilinear interactions produce a relatively simple off-diagonal pattern of the matrix of second derivatives.

Lifetime of skyrmions and antiskyrmions

In this section we discuss numerically obtained observables, including the radius (Fig. 2d), the energy barrier (Fig. 2e), the pre-exponential factor (Fig. 2f) and the lifetimes (Fig. 2g, h) of skyrmions and antiskyrmions in Pd/Fe/Ir(111) as a function of the magnetic field for two cases: with and without explicit HOI. The radius—obtained through a fit of a theoretical profile[66] to

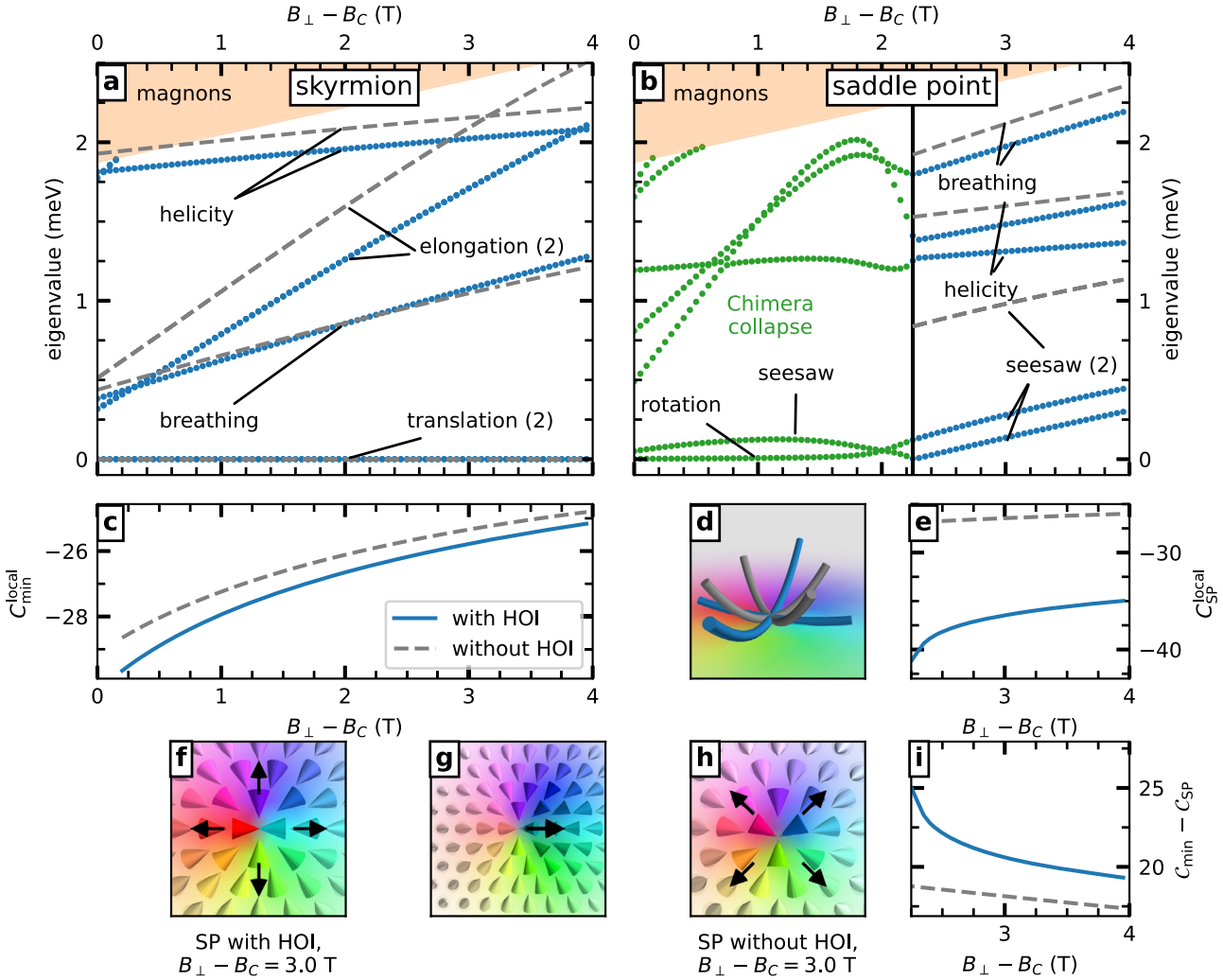


Fig. 3 | HOI and curvature of the energy surface for the skyrmion. Local part of the eigenvalue spectrum of the Hessian matrix of the skyrmion (**a**, blue) and the skyrmion saddle point (SP) (**b**, green and blue) in fcc-Pd/Fe/Ir(111) including HOI as a function of the magnetic field $B_\perp - B_C$. Eigenvalues above the magnon gap are indicated by the orange painted area. For reference the corresponding local eigenvalue spectra in the model without considering HOI explicitly are shown as gray dashed lines. Selected eigenmodes are labeled while the number in brakets gives their multiplicity (see surrounding text). Curvature associated with the local eigenvalue spectrum (see Eq. (10)) for the skyrmion (blue, **c**) and the corresponding SP (blue, **e**) for the energy model including HOI (solid line). The local curvatures of the skyrmion and the SP for the model neglecting HOI are drawn with dashed gray lines. In **e** only the regime of the radial collapse is shown. **d** Energy along the seesaw eigenmodes of the SP including HOI (blue, SP in **f**) and of the SP excluding HOI (gray, SP in **h**). **g** Configuration obtained after displacing the SP in **f** along the indicated direction (black arrow) using the corresponding eigenvector of the seesaw mode. **i** Total curvature difference of the minimum and the SP for the regime of the radial collapse mechanism.

the magnetic texture—increases upon the explicit inclusion of HOI (Fig. 2d) but still the skyrmions and antiskyrmions are of the size of few nanometers agreeing well with experimental data[16,18,58].

For the energy barrier, pre-exponential factor, and lifetimes, identifying the relevant first-order SP—characteristic of the respective collapse mechanism—is crucial. We compute SPs for annihilations of metastable states for various magnetic fields in the FM phase ($B_\perp > B_C$) using the GMMF method[67] (see "Methods"). When HOI are taken into account explicitly, the skyrmion annihilation proceeds via a Chimera collapse[17,18] for magnetic fields satisfying $B_\perp - B_C < 2.25$ T. The corresponding SP at a field of $B_\perp - B_C = 1.25$ T is shown in Fig. 2a. At higher magnetic fields, the more commonly observed radial collapse mechanism[37,60,68,69] occurs, as illustrated in Fig. 2b for $B_\perp - B_C = 3.25$ T. This SP can be characterized by four magnetic moments forming a Bloch point-like defect.

Within the explored parameter range, the collapse mechanism of the antiskyrmion corresponds to a radial shrinking of the configuration from the energy minimum (Fig. 2c). The energy barriers for the collapse of the skyrmions and antiskyrmions are shown in Fig. 2e. For comparison, the corresponding barriers obtained in the model neglecting HOI are also included. In agreement with ref. 41, explicitly considering HOI increases the energy barriers by approximately 100 meV for fcc-Pd/Fe/Ir(111).

To quantify the thermal stability of skyrmions and antiskyrmions at a given temperature T the mean-lifetime τ is computed using Eq. (2)[69,70] (see "Methods"). In magnetic systems, the entropic contribution—contained in the pre-exponential factor ν_0—can vary by several orders of magnitude as a function of the magnetic field[55,59]. Thus, it is essential to consider this factor explicitly. Figure 2f shows the pre-exponential factor divided by the temperature as a function of the magnetic field $B_\perp - B_C$. Explicitly including HOI yields pre-exponential factors slightly increased but of the same order of magnitude for skyrmions, and approximately one order of magnitude larger for antiskyrmions, compared to the model neglecting HOI. This consequently has to be related to effects on the curvature of the energy surface, as discussed in the next section. It should be noted that the pre-exponential factor is only shown in the regime $B_\perp - B_C \geq 2.25$ T, where the radial collapse mechanism of the skyrmion is favored (Fig. 2f).

Using HTST considering both the effect of the energy barrier and the entropic contributions contained in the pre-exponential factor in Eq. (2), the mean lifetime of skyrmions (Fig. 2g) and antiskyrmions (Fig. 2h) is evaluated across a range of temperatures and for varying $B_\perp - B_C$. Comparison with the iso-lifetime line corresponding to one-hour in the model where we neglect HOI demonstrates that the explicit consideration of HOI leads to substantially increased thermal stability for both skyrmions and antiskyrmions. While skyrmions remain stable for at least one hour at $T = 50$ K within the considered field range when HOI are included, the temperature must be reduced to $T < 30$ K to achieve comparable stability in the model neglecting HOI. Furthermore, while the antiskyrmions are only stable up to fields of $B_\perp - B_C \approx 2.7$ T without HOI, explicit consideration of HOI yields antiskyrmion lifetimes of at least one hour for temperatures $T \leq 20$ K in the field range of $B_\perp - B_C \approx 3$ T to $B_\perp - B_C \approx 4$ T. Thus, we record a beneficial effect of HOI on the lifetime and robustness of metastable magnetic states in this material. We have performed similar calculations for fcc-Pd/Fe/Rh(111) leading to qualitatively similar results presented in Supplementary Fig. 1.

Curvature of the energy surface

The curvature of the energy surface in the vicinity of stationary points determines the entropic contributions to the lifetime of meta-stable configurations (Eq. (2)) as sketched in Fig. 1d. Here, we explain the increased pre-exponential factor ν_0 when HOI are explicitly included (cf. Fig. 2f), compared to the case in which HOI are neglected. Figure 3a, b present the eigenvalues of the Hessian of the energy (see Eq. (15)) as functions of the magnetic field $B_\perp - B_C$ for the skyrmion (Fig. 3a) and for the SP (Fig. 3b) associated with skyrmion collapse in the fcc-Pd/Fe/Ir(111) system. For each stationary point, we divide the eigenspectrum into eigenmodes with eigenvalues below and above the boundary of the magnon gap. For the Hamiltonian in Eq. (3) this gap reads:

$$\epsilon_{\mathrm{mag}} = \mu B_\perp + 2K_u \,. \tag{8}$$

Eigenvalues below ϵ_{mag} correspond to excitations of the localized magnetic texture in the FM background and are referred to as local part of the eigenspectrum. For the skyrmion, this local spectrum includes two zero modes (translations), a breathing mode, two degenerate elongation modes, and a helicity mode (see "Methods") The eigenvalue spectrum of the skyrmion including HOI closely resembles that of the skyrmion in the model without HOI[55], depicted as dashed gray lines in Fig. 3a. Quantitatively, the eigenvalues of the rotation and elongation modes of the skyrmion shift to lower values when HOI are explicitly included.

Considering HOI explicitly favors the Chimera collapse as the dominant skyrmion annihilation mechanism for $B_\perp - B_C \leq 2.25$ T, as shown in Fig. 2e. The Chimera SP features a rotation mode (a zero mode) and a low-curvature seesaw mode. This name was chosen since following this mode leads to a 180°-rotated Chimera SP via a configuration which is very similar to the radial SP and in fact constitutes a second-order SP on the energy landscape. Since HTST requires a clear separation between first- and second-order SPs, calculating the prefactor in this regime is technically challenging. We present results for the pre-exponential factor of the Chimera collapse for the case of an applied in-plane magnetic field in Supplementary Note 3 and Supplementary Figs. 2, 3 and 4, since the main focus of this paper is the effect of HOI on lifetimes and the Chimera collapse has been discussed elsewhere[18].

However, the seesaw mode is also relevant for the radial collapse regime. At $B_\perp - B_C = 2.25$ T, its eigenvalue approaches zero, signaling a flat energy landscape between the Chimera and radial SPs, reminiscent of a second-order phase transition[71]. For higher fields, the radial SP becomes a first-order SP with two non-degenerate seesaw eigenvalues (Fig. 3b). This SP (Fig. 3f) can be characterized by four magnetic moments, placed at the four vertices of a diamond, pointing toward each other. The seesaw eigenmodes act as a deformation of the diamond-like SP configuration (Fig. 3f) into asymmetric states along the diagonals of the diamond (Fig. 3g). Since eigenvalues are directly associated with the curvature of the energy landscape the situation can be visualized by the parabolic energy dependence along the eigenvectors of the two seesaw eigenmodes which is shown in Fig. 3d in blue.

In contrast, neglecting HOI yields degenerate and larger seesaw eigenvalues (Fig. 3b, dashed gray lines), consistent with the triangular SP configuration (Fig. 3h) that preserves lattice symmetry and explains the degeneracy (Fig. 3h, gray). Overall, explicit HOI reduce the curvature of the seesaw modes, because the 4-site HOI energetically favors the deformation of the radially-symmetric SP state into the asymmetric configuration along the seesaw mode as shown in Supplementary Note 4 and Supplementary Fig. 5. Explicit HOI also lower the helicity and breathing eigenvalues, similar to the shifts observed for the skyrmion elongation and helicity modes upon consideration of explicit HOI.

We define a measure $\mathcal{C}$ for curvature of the energy landscape at the minimum ($\mathcal{C} = \mathcal{C}_{\mathrm{min}}$) and the SP ($\mathcal{C} = \mathcal{C}_{\mathrm{SP}}$) excluding zero-modes, which are identified below the threshold $\delta_{\mathrm{zero}} = 10^{-12}$ eV, and the unstable mode of the SP with $\epsilon_1^{\mathrm{SP}} < 0$. Further, in order to identify thermodynamically relevant parts of the spectrum, we distinguish between local and magnon contributions, separated by ϵ_{mag} from Eq. (8):

$$\mathcal{C} = \mathcal{C}^{\mathrm{local}} + \mathcal{C}^{\mathrm{magnon}} \tag{9}$$

$$\mathcal{C} = \sum_{\delta_{\mathrm{zero}} < \epsilon_k < \epsilon_{\mathrm{mag}}} \ln \frac{\epsilon_k}{\epsilon_0} + \sum_{\epsilon_k \geq \epsilon_{\mathrm{mag}}} \ln \frac{\epsilon_k}{\epsilon_0} \,, \tag{10}$$

where an energy scale $\epsilon_0 = 1$ eV was introduced to ensure dimensionless expressions in the logarithms. This establishes an intuitive connection between curvatures and the entropy from Eq. (7), which explicitly reads:

$$\frac{\Delta \mathcal{S}}{k_B} = \frac{\mathcal{C}_{\mathrm{min}} - \mathcal{C}_{\mathrm{SP}}}{2} + \ln \left[\frac{V^{\mathrm{SP}}}{V^{\mathrm{min}}} \left(\frac{2\pi}{\beta \epsilon_0} \right)^{\frac{\Delta Z}{2}} \right] . \tag{11}$$

As shown in Fig. 3c, e, the curvature of the local part of the spectrum at the minimum is nearly unaffected by HOI, whereas the local curvature at the SP is strongly reduced due to shift of the localized eigenmodes of the SP, particularly the seesaw eigenmodes. Since SP curvature enters Eq. (11) with a negative sign, this reduction, caused by HOI, enhances the annihilation rate. Including contributions above the magnon gap (Fig. 3i) reproduces the field dependence of the pre-exponential factor (Fig. 2f). However, it can be seen that the difference between both models is smaller in Fig. 3i than in Fig. 3e. This implies that the curvature contribution of the eigenspectrum above the magnon gap counteracts —but not compensates—the entropic destabilization by the eigenvalues of the local spectrum that are reduced upon explicit consideration of HOI. In Supplementary Note 5 and Supplementary Fig. 6 we present a similar discussion for the curvature of the energy surface for the antiskyrmion collapse.

Tuning the 4-site HOI interaction

Now we turn to the influence of variations in the 4-site HOI parameter K_1 (see Eq. (3)) on the lifetimes of skyrmions (Fig. 4b) and antiskyrmions (Fig. 4d) with respect to thermally activated annihilation into the FM state. Since spin spiral energies are degenerate with respect to the 4-site HOI parameter, the parametrization of the bilinear interaction constants obtained in DFT remains valid even if K_1 is varied[41]. This allows us to analyze the role of the 4-site HOI in stabilizing topological magnetic textures. In ref. 41, a linear dependence of the energy barriers on K_1 was reported for both skyrmions and antiskyrmions. Our calculations reproduce this behavior (Fig. 4a, c). While skyrmions remain metastable even for negative K_1, the energy barrier for antiskyrmions vanishes as $K_1 \to 0$ meV.

Here, we also compute the pre-exponential factor for skyrmions and antiskyrmions as a function of K_1. We find that the pre-exponential factor for antiskyrmions (Fig. 4c) remains nearly constant across the considered range, whereas for skyrmions it decreases by about three orders of magnitude upon reducing K_1 (Fig. 4a). The local part of the Hessian eigenmode spectrum for the skyrmion and the SP is shown in Supplementary Fig. 7 as a function of the 4-site HOI parameter. Noteworthy, HTST is valid

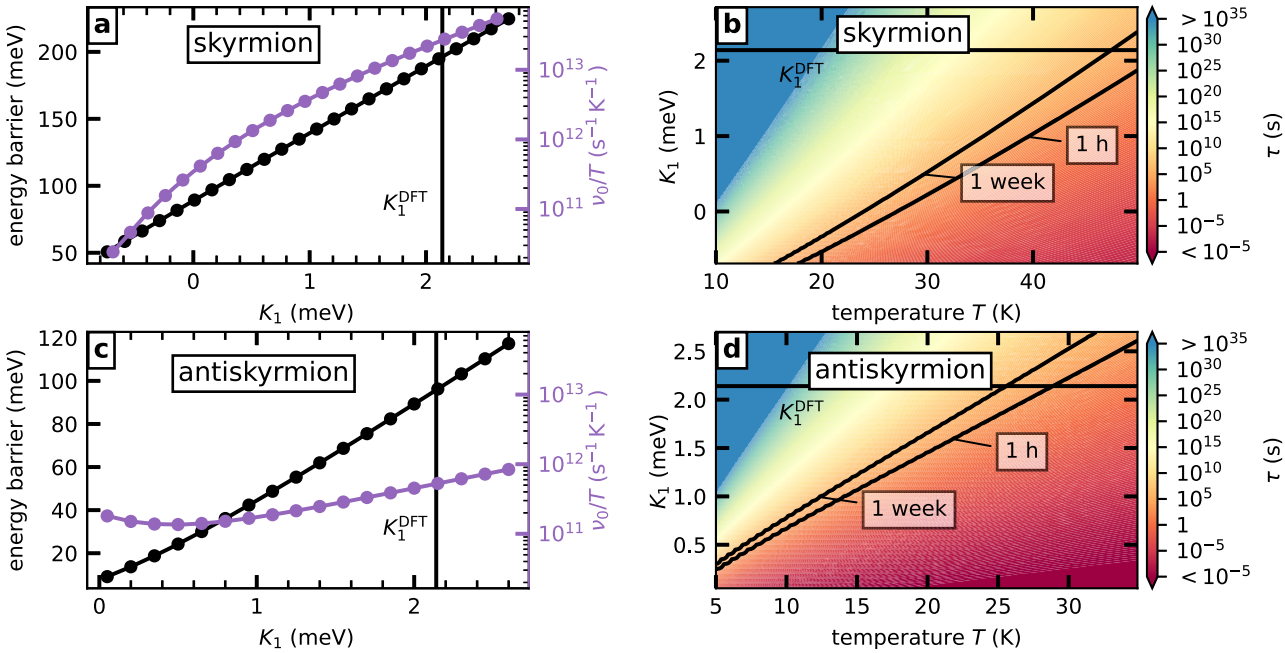


Fig. 4 | Lifetimes of skyrmions and antiskyrmions as a function of the 4-site HOI. **a**, **c** Energy barrier (black) and pre-exponential factor ν_0/T (purple) for the skyrmion (**a**) and the antiskyrmion (**c**) annihilation in fcc-Pd/Fe/Ir(111) for a magnetic field of $B_\perp = 6$ T (skyrmions) and $B_\perp = 4$ T (antiskyrmions) as a function of the 4-site HOI K_1. The value K_1^{DFT} corresponds to the one determined in DFT calculations[41]. Mean lifetime τ for isolated skyrmions (**b**) and antiskyrmions (**d**) for various temperatures T and values of K_1 calculated within HTST. The one-week- and one-hour-isoline of τ are given as black lines.

throughout the considered range of K_1 as none of the eigenvalues strives toward zero. The change of pre-exponential factor and energy barrier with strength of the 4-site HOI, leads to opposite effects on the thermal stability of skyrmions. While the increase of the energy barrier with K_1 also leads to an enhanced lifetime, the increase of the pre-exponential factor results in a decrease of the lifetime as seen from the Arrhenius law (cf. Eq. (2)). Note that the variation of K_1 within the considered range $K_1 \in [-0.75, 2.7]$ meV represents realistic values for the 4-site HOI in transition-metal thin film systems[41,51,62,72].

The lifetime of skyrmions (Fig. 4b) and antiskyrmions (Fig. 4d) changes drastically upon variation of K_1. For instance, at $T = 40$ K the predicted lifetime of a skyrmion with $K_1 = 1.0$ meV is about 45 minutes. Increasing K_1 by only 0.5 meV extends the lifetime to roughly 18 days. The effect of HOI on the stability is also visible from the increase of the temperature for a given lifetime. For example, a mean lifetime of above one hour is obtained below a temperature of about 30 K for $K_1 = 0$ and increases to above 40 K for a small 4-site 4-spin term of $K_1 = 1$ meV. For antiskyrmions, we observe a similar trend, however, at overall shorter lifetimes at a given temperature due to the lower energy barriers (Fig. 4c).

Skyrmions and antiskyrmions without DMI

Designing systems hosting isolated skyrmions with maximum thermal stability typically requires large DMI constants and/or exchange frustration. In ref. 41, it was predicted that both skyrmions and antiskyrmions are metastable when HOI are explicitly included, even in the absence of DMI, based on calculations of the energy barriers for their collapse into the FM state. However, thermal stability cannot be deduced from the barrier height alone. In this section, we present the calculated pre-exponential factor in the Arrhenius law and the corresponding mean lifetime for fcc-Pd/Fe/Ir(111), including HOI but neglecting DMI (see Fig. 5). The isolated skyrmion and its topological counterpart, the antiskyrmion, exhibit significant and identical energy barriers for their collapse into the FM state (Fig. 5a) consistent with previous work[41]. The origin of the energy barrier is nearly entirely due to the effect of the 4-site HOI while the exchange frustration contributes only little.

In addition, we quantify the pre-exponential factors and demonstrate that they are also degenerate when DMI is neglected (Fig. 5a). The values obtained for the pre-exponential factor are basically independent of the applied magnetic field and of a similar order of magnitude as previously reported for skyrmions in ultrathin films including DMI[55]. This independence can be related to the skyrmion and antiskyrmion radius (Fig. 5b), which is only changing little upon variation of the applied field. Neglecting DMI leads to smaller values of the radius of skyrmions and antiskyrmions and to a weaker field-dependence of the size compared to the radius of these textures including DMI (cf. Fig. 2d). Furthermore, the SP configurations corresponding to the annihilation of these textures into the FM state consist of only a few magnetic moments forming the Bloch point-like defect and consequently their size also does not change upon variation of the applied field. Since the size and the shape of the configurations of the minima and the SPs change only little, the curvature values of the energy landscape at the stationary points, expressed by the respective eigenvalues of the Hessian, and consequently also the pre-exponential factors show a minor dependence on the applied magnetic field. The corresponding eigenvalue spectra for the skyrmion and antiskyrmion—again degenerate—and the SP when neglecting DMI but explicitly considering HOI are presented in Supplementary Note 6 and Supplementary Fig. 8.

Since the pre-exponential factors are the same for skyrmions and antiskyrmions, their mean lifetimes—as obtained from HTST—are also identical (Fig. 5c). Note, that in the case of skyrmions in a Hamiltonian without DMI the helicity mode of the minimum and the SP configuration becomes a zero mode[36,40] ("Methods"). The results in Fig. 5c indicate that skyrmions and antiskyrmions remain metastable over a broad range of magnetic fields $B_\perp - B_C$, at timescales and temperatures relevant to low temperature STM experiments, even in the absence of DMI.

Discussion

In this work, we have investigated the effect of higher-order exchange interactions (HOI) on the lifetimes of isolated skyrmions and antiskyrmions in fcc-Pd/Fe/Ir(111) and fcc-Pd/Fe/Rh(111), focusing on their thermally activated annihilation into the FM state. By implementing general fourth-order HOI terms for the energy, gradient and Hessian of the system into our atomistic spin simulations code, we are able to provide a comprehensive, quantitative description of these lifetimes within the framework of HTST.

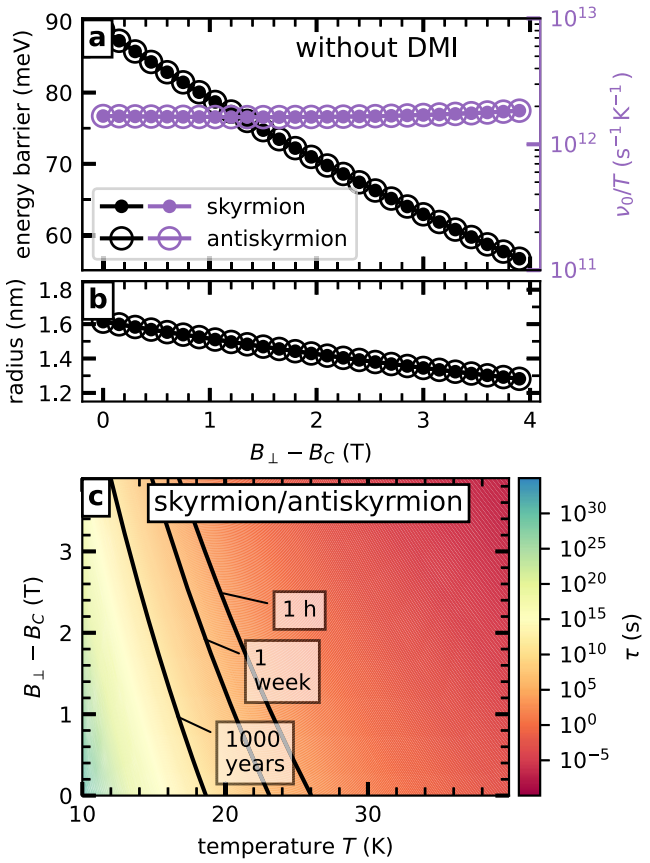


Fig. 5 | Skyrmion and antiskyrmion lifetime including HOI and neglecting DMI. **a** Energy barriers (black) and pre-exponential factors ν_0 (purple) of skyrmions (filled circles) and antiskyrmions (open circles) in fcc-Pd/Fe/Ir(111) considering HOI and vanishing DMI for varying the magnetic field relative to the critical field $B_\perp - B_C$. **b** Radius of skyrmions and antiskyrmions as a function of the magnetic field. **c** Mean lifetime τ (see colorbar) of the above mentioned isolated magnetic textures as a function of the temperature T and the external magnetic field $B_\perp - B_C$.

This enables a quantitative description of lifetimes in systems with HOI that goes well beyond simple energy-barrier arguments for the stability of skyrmions and antiskyrmions. Since HOI can play a key role in many materials such as transition-metal interfaces[15,41,47,48,50,51,62] and 2D van der Waals magnets and heterostructures[28–31,64] our results present an important step towards realistic stability predictions for topological magnetic textures in these systems.

The enhanced energy barriers observed upon explicitly considering HOI lead to markedly increased lifetimes of skyrmions and antiskyrmions (see Fig. 2e, g, h), which has important implications for the design of robust topological magnetic bits. Furthermore, we report a slight reduction of the stability of skyrmions and antiskyrmions due to changed entropic contributions when including HOI in materials that are subject to our investigation (Fig 2f). We were able to identify the origin of the increased pre-exponential factor for the skyrmion collapse as a reduced curvature of the energy landscape due to the local Hessian eigenvalue spectrum at the SP (see Fig. 3c, e, i). The dynamic contributions to the pre-exponential factor change only little upon considering HOI explicitly.

For both cases—the skyrmion and the antiskyrmion collapse—the HOI terms affect the curvature in the direction of the localized excitations at the SP significantly more than the corresponding curvatures at the minimum. These SP configurations exhibit larger canting angles between adjacent magnetic moments than the minima. Since the contribution of the HOI terms to the energy is strongly affected by strong canting of the magnetization this is likely to be the origin of the pronounced effect of HOI on the energy landscape at the SP. This makes entropic stabilization by HOI, due to increased (decreased) curvature of the energy surface at the SP (minimum), a promising route to engineer skyrmion and antiskyrmion stability.

A particularly striking result is the sensitivity of lifetimes to the 4-site interaction parameter K_1, which underlines the critical role of HOI in determining skyrmion and antiskyrmion stability. It also suggests that targeted manipulation of K_1, for example by material choice or interface engineering, could provide a powerful strategy to design skyrmions with lifetimes tailored for specific experimental or technological applications. Remarkably, our study reveals a strong dependence of the pre-exponential factor on the strength of the 4-site interaction for skyrmions. This suggests that accurate lifetime predictions require full entropic modeling rather than assuming a constant prefactor. The sensitivity of skyrmion and antiskyrmion stability on K_1 is also interesting for future work in the light of quenched disorder[73], e.g due to impurities or adatoms[74] or lattice mismatch in Moiré systems[75].

Finally, we also predict that both skyrmions and antiskyrmions remain metastable in the complete absence of DMI—stabilized almost entirely by HOI—at timescales and temperatures relevant to experiments. While switching off the DMI in fcc-Pd/Fe/Ir(111) represents a toy model, this limit is physically motivated by a growing class of centrosymmetric magnetic systems where DMI is symmetry-suppressed. In particular, it has been demonstrated by first-principles calculations for several centrosymmetric two-dimensional van der Waals magnets, such as transition-metal phosphorous trichalcogenides, that higher-order exchange interactions play a significant role for their magnetic properties[28,29,76]. Our results therefore highlight HOI as a viable alternative stabilization mechanism for topological magnetic textures in materials with inversion symmetry or without heavy elements providing strong spin-orbit coupling, and suggest a realistic pathway toward skyrmionic textures in emerging 2D magnetic materials. Furthermore, it is likely that engineering materials explicitly in the regard of significant HOI impacts the stability of magnetic textures beyond skyrmions such as bimerons or skyrmionium.

Methods

Energy parameters for the spin model

The energy parameters employed in the atomistic spin model were obtained from density functional theory calculations[77,78] and adopted from the literature. Detailed computational procedures and results for structural relaxations, exchange interactions, Dzyaloshinskii-Moriya interaction (DMI), magnetocrystalline anisotropy energy (MAE), and magnetic moments are reported in ref. 37 for Pd/Fe/Ir(111) and in ref. 61 for Pd/Fe/Rh(111). Calculations of higher-order exchange interactions for both systems are presented in ref. 41. The interaction parameter values are given in Supplementary Note 1 and Supplementary Tables 1 and 2.

Calculation of the pre-exponential factor

The mean-lifetime τ for thermally activated annihilation of skyrmions and antiskyrmions into the FM state are computed in this work using the Arrhenius law (Eq. (2)) within the framework of harmonic transition state theory (HTST)[70]. In HTST the transition state for a particular reaction mechanism described by an MEP connecting two minima (skyrmion/antiskyrmion and FM state) is chosen as the hyperplane through a first order SP perpendicular to its unstable mode. This SP is the configuration of highest energy along the MEP. The contributions to the Arrhenius law are, on the one hand, the energy barrier ΔE, which is given as the energy difference of the SP and the energy minimum configuration (see Eq. (5)). On the other hand, the pre-exponential factor ν_0 is given by the entropic and the dynamic contribution λ to the transition (Eq. (6)), which are calculated based on the complete spectrum of eigenmodes at the stationary points and by linearizing the Landau-Lifshitz equation at the SP[56].

Note, that while several formulations exist for the pre-exponential factor[55,60,70], Eq. (6) is particularly useful to discuss entropic effects (Eq. (7)). While almost all degrees of freedom are treated in harmonic approximation, translations, rotations or modes changing the helicity of the localized magnetic texture are often better treated in Goldstone mode approximation[40,55,69] and their contribution to the entropy then corresponds to the zero mode volume

V. Additionally, a factor ρ for the multiplicity of identical SP per unit cell[55] is required. In this work, it is either $\rho = 1$ or $\rho = 2$. Supplementary Note 7, Supplementary Fig. 9 and Supplementary Table 3 present the values of ρ of the pre-exponential factor calculations of this work. Note, that the helicity degree of freedom of the skyrmion in the HOI model neglecting DMI, for which the pre-exponential factor is shown in Fig. 5a, is also a zero mode with volume[40]

$$V_{\mathrm{hel}} = 2\pi \sum_{n=1}^{N} \left[1 - (m_n^z)^2\right] . \tag{12}$$

The respective degree of freedom describes the continuous deformation between Néel- and Bloch-type skyrmions, which comes down to a collective rotation of all spins in the $xy-$ plane.

Identification of first order saddle points

It is essential to identify the corresponding SP in order to calculate the energy barrier and the pre-exponential factor of the skyrmion and antiskyrmion collapse into the FM state. In this work, these SPs are determined by combining the geodesic nudged elastic band method (GNEB)[79] with the recently developed geodesic minimum mode following method (GMMF)[67]. The GNEB method was used to determine the skyrmion or antiskyrmion collapse mechanism and the SP for the maximum magnetic field considered for the specific parameter set ($B_\perp - B_C = 4$ T). Subsequently, the GMMF method was initialized using this SP and the magnetic field was reduced by a small amount of $\Delta B = 0.05$ T.

In contrast to the GNEB method, in which the GNEB force for a series of replicas of the system (path) is minimized, the GMMF method operates on a single magnetic configuration. The GMMF force corresponds to the negative energy gradient where the direction of the gradient is inverted along the direction of the minimum mode of the Hessian of the energy:

$$\mathbf{F}_{\mathrm{GMMF}} = -\nabla E + 2(\nabla E \cdot \mathbf{v}_1)\mathbf{v}_1 . \tag{13}$$

This yields a minimization of the energy along all degrees of freedom except one, while the energy is maximized along the direction of the eigenvector $\mathbf{v}_1$ of the minimum mode. If the GMMF method is initialized with a configuration in the vicinity of an SP, it converges to a first order SP within a few iterations. The computational bottleneck is the repeated calculation of the eigenvector of the lowest eigenvalue of the Hessian matrix of the energy of the system.

Recently, we introduced Rayleigh Quotient minimization[67], a method that makes an efficient calculation of the minimum mode feasible and is based on finite difference calculations of the energy gradient without the need for the explicit calculation of the Hessian matrix. The efficient combination of these methods allowed us to calculate the activation energies with a high resolution with respect to the values of the magnetic field with almost negligible computational effort.

Hessian matrix including HOI

This section describes the calculation of the Hessian matrix for general fourth-order HOI, which is required to determine the pre-exponential factors of the skyrmion and antiskyrmion collapse. We approximate the energy surface $E(\mathbf{m})$ on the $2N$-dimensional configuration space $\mathbf{m} \in \bigotimes_n^N \mathbb{S}^2$ up to second order in the vicinity of critical points $\mathbf{m}_0$. Since first order terms vanish in these points the series expansions in terms of tangential deflections $\delta\mathbf{m}$ reads

$$E(\mathbf{m}_0, \delta\mathbf{m}) = E(\mathbf{m}_0) + \frac{1}{2}\delta\mathbf{m}^T H \delta\mathbf{m} + \mathcal{O}(\delta\mathbf{m}^3) . \tag{14}$$

Due to the constraint of magnetic moments having fixed length the Hessian $H \in \mathbb{R}^{2N\times 2N}$ is constrained to the tangent space of the magnetic configuration:

$$H_{ij} = P_i(\nabla_{ij}\mathcal{L})P_j^T , \ \mathcal{L} = E - \sum_{i=1}^{N}(\mathbf{m}_i^2 - 1)\omega_i \tag{15}$$

with the Lagrange function $\mathcal{L}$ and Lagrange multipliers $\omega_i = \mathbf{m} \cdot \nabla_i E/2$. Here $\nabla_i = \frac{\partial}{\partial \mathbf{m}_i}$ and $\nabla_{ij} = \nabla_i \nabla_j^{\mathrm{T}}$ are the partial derivatives with respect to the coordinates of the magnetic moment $\mathbf{m}_i$ and $P_i \in \mathbb{R}^{2\times 3}$ is the projection on the tangent space of $\mathbf{m}_i$[56,68]. In our setup derivatives of the Lagrange multiplier ω_i can be omitted, because they describe changes of the energy under variation of the spin length. Thus, they are perpendicular to the manifold associated with configuration space and vanish in the quadratic form of Eq. (14), since they are perpendicular to tangential deflections $\delta\mathbf{m}$.

While bilinear interactions between magnetic moments have been considered extensively in the framework of HTST[40,55,56,60,69], the novelty of this work is the consideration of HOI (cf. Eq. (1)). Gradients with respect to coordinates of magnetic moments are computed as

$$\nabla_i E_{4-\mathrm{spin}} = -4 \sum_{jkl} C_{ijkl}(\mathbf{m}_k \cdot \mathbf{m}_l)\mathbf{m}_j . \tag{16}$$

Similar to bilinear exchange $E_{\mathrm{exc}} \propto \mathbf{m}_i^T \underline{J}_{ij} \mathbf{m}_j$ being mediated by a tensor $\underline{J}_{ij} \in \mathbb{R}^{3\times 3}$, HOI are mediated by a tensor $\underline{C}_{ijkl} \in \mathbb{R}^{3\times 3\times 3\times 3}$. Since both the bilinear exchange as well as HOI are invariant under global rotation of all magnetic moments, and therefore isotropic in configuration space, the HOI tensor can be expressed in the basis of isotropic tensors of fourth-order, which are usually denoted as products of Kronecker δ symbols

$$\underline{C}_{ijkl} = C_{ijkl}\delta_{ij}\delta_{kl} \tag{17}$$

with interaction constant C_{ijkl}. It is commonly known that this basis contains only two more linearly independent elements, $\delta_{ik}\delta_{jl}$ and $\delta_{il}\delta_{kj}$, which in our case correspond to certain permutations of indices (i, j, k, l). In matrix form these tensors can be constructed as

$$\begin{aligned}
\delta_{ij}\delta_{kl} &= \begin{bmatrix} \begin{bmatrix} 1&0&0\\0&1&0\\0&0&1 \end{bmatrix} & \begin{bmatrix} 0&0&0\\0&0&0\\0&0&0 \end{bmatrix} & \begin{bmatrix} 0&0&0\\0&0&0\\0&0&0 \end{bmatrix} \\ \begin{bmatrix} 0&0&0\\0&0&0\\0&0&0 \end{bmatrix} & \begin{bmatrix} 1&0&0\\0&1&0\\0&0&1 \end{bmatrix} & \begin{bmatrix} 0&0&0\\0&0&0\\0&0&0 \end{bmatrix} \\ \begin{bmatrix} 0&0&0\\0&0&0\\0&0&0 \end{bmatrix} & \begin{bmatrix} 0&0&0\\0&0&0\\0&0&0 \end{bmatrix} & \begin{bmatrix} 1&0&0\\0&1&0\\0&0&1 \end{bmatrix} \end{bmatrix} \\
\delta_{ik}\delta_{jl} &= \begin{bmatrix} \begin{bmatrix} 1&0&0\\0&0&0\\0&0&0 \end{bmatrix} & \begin{bmatrix} 0&1&0\\0&0&0\\0&0&0 \end{bmatrix} & \begin{bmatrix} 0&0&1\\0&0&0\\0&0&0 \end{bmatrix} \\ \begin{bmatrix} 0&0&0\\1&0&0\\0&0&0 \end{bmatrix} & \begin{bmatrix} 0&0&0\\0&1&0\\0&0&0 \end{bmatrix} & \begin{bmatrix} 0&0&0\\0&0&1\\0&0&0 \end{bmatrix} \\ \begin{bmatrix} 0&0&0\\0&0&0\\1&0&0 \end{bmatrix} & \begin{bmatrix} 0&0&0\\0&0&0\\0&1&0 \end{bmatrix} & \begin{bmatrix} 0&0&0\\0&0&0\\0&0&1 \end{bmatrix} \end{bmatrix} \\
\delta_{il}\delta_{kj} &= \begin{bmatrix} \begin{bmatrix} 1&0&0\\0&0&0\\0&0&0 \end{bmatrix} & \begin{bmatrix} 0&0&0\\1&0&0\\0&0&0 \end{bmatrix} & \begin{bmatrix} 0&0&0\\0&0&0\\1&0&0 \end{bmatrix} \\ \begin{bmatrix} 0&1&0\\0&0&0\\0&0&0 \end{bmatrix} & \begin{bmatrix} 0&0&0\\0&1&0\\0&0&0 \end{bmatrix} & \begin{bmatrix} 0&0&0\\0&0&0\\0&1&0 \end{bmatrix} \\ \begin{bmatrix} 0&0&1\\0&0&0\\0&0&0 \end{bmatrix} & \begin{bmatrix} 0&0&0\\0&0&1\\0&0&0 \end{bmatrix} & \begin{bmatrix} 0&0&0\\0&0&0\\0&0&1 \end{bmatrix} \end{bmatrix}
\end{aligned} \tag{18}$$

In this notation the indices i, j address the position of each 3 × 3-matrix within the tensors above. The indices k, j address the position of 1 or 0 within these submatrices. Note, that other representations of this basis exist as well. Intuitively, the linearly independent basis elements reflect that some permutations of lattice sites in fourth-order HOI lead to different energies

$$\begin{aligned}(\mathbf{m}_i \cdot \mathbf{m}_j)(\mathbf{m}_k \cdot \mathbf{m}_l) &\neq (\mathbf{m}_i \cdot \mathbf{m}_k)(\mathbf{m}_j \cdot \mathbf{m}_l) \\ &\neq (\mathbf{m}_i \cdot \mathbf{m}_l)(\mathbf{m}_k \cdot \mathbf{m}_j)\end{aligned} \tag{19}$$

while linear dependent permutations leave the energy invariant

$$\begin{aligned}(\mathbf{m}_i \cdot \mathbf{m}_j)(\mathbf{m}_k \cdot \mathbf{m}_l) &= (\mathbf{m}_k \cdot \mathbf{m}_l)(\mathbf{m}_i \cdot \mathbf{m}_j) \\ &= (\mathbf{m}_l \cdot \mathbf{m}_k)(\mathbf{m}_j \cdot \mathbf{m}_i)\,.\end{aligned} \tag{20}$$

In order to find the most general form of second derivatives of the fourth-order HOI energy with respect to $\mathbf{m}_i$ and $\mathbf{m}_j$ all linearly independent permutations have to be considered

$$\begin{aligned}\nabla_{ij} E_{4-\mathrm{spin}} &= \sum_{kl} \mathbf{m}_k^T (C_{ijkl}\delta_{ij}\delta_{kl} + C_{ikjl}\delta_{ik}\delta_{jl} \\ &\quad + C_{ilkj}\delta_{il}\delta_{kj})\mathbf{m}_l\end{aligned} \tag{21}$$

$$\begin{aligned}&= \sum_{kl} (C_{ijkl}\,\mathbf{m}_k \odot \mathbf{m}_l + C_{ikjl}\,\mathbf{m}_l \otimes \mathbf{m}_k \\ &\quad + C_{ilkj}\,\mathbf{m}_k \otimes \mathbf{m}_l)\end{aligned} \tag{22}$$

where we used the abbreviations

$$\mathbf{m}_i \otimes \mathbf{m}_j = \begin{pmatrix} m_i^x m_j^x & m_i^x m_j^y & m_i^x m_j^z \\ m_i^y m_j^x & m_i^y m_j^y & m_i^y m_j^z \\ m_i^z m_j^x & m_i^z m_j^y & m_i^z m_j^z \end{pmatrix} \tag{23}$$

$$\mathbf{m}_i \odot \mathbf{m}_j = \begin{pmatrix} \mathbf{m}_i \cdot \mathbf{m}_j & 0 & 0 \\ 0 & \mathbf{m}_i \cdot \mathbf{m}_j & 0 \\ 0 & 0 & \mathbf{m}_i \cdot \mathbf{m}_j \end{pmatrix} \tag{24}$$

The step between Eq. (21) and Eq. (22) involves quadratic forms of spins with every 3 × 3-submatrix denoted within the tensors of Eq. (18)[57]. Since the last two terms in Eq. (22) are related by $\mathbf{m}_k \otimes \mathbf{m}_l = (\mathbf{m}_l \otimes \mathbf{m}_k)^T$ (transposing inverts order of magnetic moments) the construction of Hessian blocks comes down to the two cases:

$$\nabla_{ij} E_{4-\mathrm{spin}} = -4 \sum_{kl} \begin{cases} C_{ijkl}\,\mathbf{m}_k \odot \mathbf{m}_l & \text{for (i, j, k, l)} \\ C_{ikjl}\,\mathbf{m}_l \otimes \mathbf{m}_k & \text{for (i, k, j, l)} \end{cases}, \tag{25}$$

where only the order of indices has to be considered, including variations with repeating indices which address 3-site and biquadratic HOI terms.

Figure 6 shows exemplarily contributions of HOI to the Hessian blocks of four magnetic moments within nearest neighbor distance to each other. It is noteworthy that $\nabla_{ij} E_{4-\mathrm{spin}} = (\nabla_{ji} E_{4-\mathrm{spin}})^T$, so that the Hessian itself is symmetric, as required on torsion-free configuration spaces.

Implementation of the HOI

General fourth-order HOI (Eq. (1)) were implemented in our atomistic spin simulation package SPINAKER for arbitrary lattice models, including three-dimensional ones. The code is capable of an efficient computation of the energy, gradients and Hessians of user-input fourth-order HOI over arbitrary distances of the lattice. Each term contributing to the general form of the fourth-order HOI, e.g. the biquadratic, 3-site or 4-site term, can be uniquely identified through an array of six distances (Eq. (4)). These distances are given in units of n-th nearest neighbor distances between the atomic sites of the respective lattice model. Based on this adjacency information the neighbor relations of a specific HOI are derived in a pre-processing step through the "Pairfinder"-algorithm explained below. A pseudo-code representation of the core of the Pairfinder algorithm is given in Alg. 1.

The lattice of atoms is constructed by repetitions of the chemical unit cell containing one or more atomic species. Consider a central atomic site with index i. Figures 7a, b illustrate small 3 by 3 segments of a hexagonal lattice with an exemplary central atomic site i and an integer index assigned to each site of these nine unit cells (Fig. 7b). In Fig. 7a the Pairfinder is illustrated for the 4-site HOI (denoted by the interaction strength K in Eq. (3)). In this case, the array of distances is $[d_{ij}, d_{ik}, d_{il}, d_{jk}, d_{jl}, d_{kl}] = [1, 1, 1, 1, 2, 1]$, involving only nearest neighbors except for the connection of j and l: $d_{jl} = 2$.

The outermost loop in Alg. 1 iterates over the neighbors of the atomic site i satisfying the constraint d_{ij}. For the 4-site HOI j corresponds to a site in nearest neighbor distance to i and for the specific system in Fig. 7b we have e.g. $j = 8$ for $i = 5$. Subsequently the index shift $n_{ij} = j - i$ is stored, which is here $n_{ij} = 3$. Ascending one level in the nested loops in Alg. 1, the next loop iterates over the neighbors with the distance constraint d_{ik} and the index shift n_{ik} is stored. For the 4-site HOI term these are again the sites in nearest neighbor distance to i ($d_{ik} = 1$). Consider e.g. the atomic site with index $k = 9$ to be selected at this stage (see Fig. 7b) with $n_{ik} = 4$. Now it has to be checked whether the selected neighbors j and k of i fulfill also the distance constraint d_{jk}, which is in this case again $d_{jk} = 1$. For this purpose the neighbors k' in distance d_{jk} of j are iterated. For each candidate k' it is tested if the index shifts of the candidate sites correspond to a closed path via $n_{ij} + n_{jk'} - n_{ik} = 0$. If this equation is satisfied, as for the site k' marked on the right in Fig. 7a, we set $k = k'$ and continue. The sites marked with blue triangles are candidates for k, k' satisfying the equation above. However, if this condition is not satisfied k' is discarded and the loop over the neighbors of j in distance d_{jk} continues with the next candidate k'. The next embedded loop iterates over the neighbors of i within distance d_{il} to the site i to produce candidates for the fourth site l. For the 4-site HOI these are again the nearest neighbors of i. For each candidate l we now have to test whether it also fulfills the distance constraints d_{jl} and d_{kl}, which are $d_{jl} = 2$ and $d_{kl} = 1$ here. Similar to the procedure above this is achieved by iterating the neighbors l' of j in distance d_{jl} and iterating the neighbors l'' of k in distance d_{kl}. For each l' and l'' it is checked whether $n_{ij} + n_{jl'} - n_{il} = 0$ and $n_{ik} + n_{kl''} - n_{il} = 0$, respectively. Only if both conditions are satisfied the candidate l completes the set of the four magnetic moments searched for the specific HOI term and the six index shifts are stored.

Note, that for each specific HOI term several sets fulfilling the above conditions exist. Consider again the 4-site HOI, where the site l has to be in second nearest neighbor distance to j and in nearest neighbor distance to k. In Fig. 7a this is only satisfied by the lattice site marked with the green diamond if j and k are chosen as schematically depicted in Fig. 7. However, also the lattice sites $j = 4$ and $k = 1$ satisfy the conditions for the first three magnetic moments participating in the 4-site HOI term. This leaves the site $l = 2$ as the only option to complete this set. Iterating over lattice sites corresponding to the array of distances recursively and evaluating conditions of closed paths ensures, finding all the sets of interacting lattice sites for a specific HOI, 12 for the case of the 4-site HOI.

Given the translational symmetry of the lattice it is sufficient to calculate these relative index shifts only once for a representative atomic site i. Thus, the computational complexity of this pre-processing step is negligible with respect to the thousands of energy and energy gradient calculations employed in a typical simulation, e.g. an iterative energy minimization algorithm.

Note, that the above representation uses single integer indices to address atomic sites and represent relative positions of sites for the sake of clarity. However, in practice SPINAKER stores multi-indices $(i_{\mathbf{a}_1}, i_{\mathbf{a}_2}, i_{\mathbf{a}_3}, i_{\mathrm{species}})$ addressing a site via the coefficients of the linear combination of lattice vectors to reach its unit cell together with a unique index of the atomic species within this cell. This allows to detect neighbors connected via periodic boundaries. These are handled with a precomputed lookup mask storing for each site whether a neighbor is present or not, which allows also to simulate defects and missing atoms.

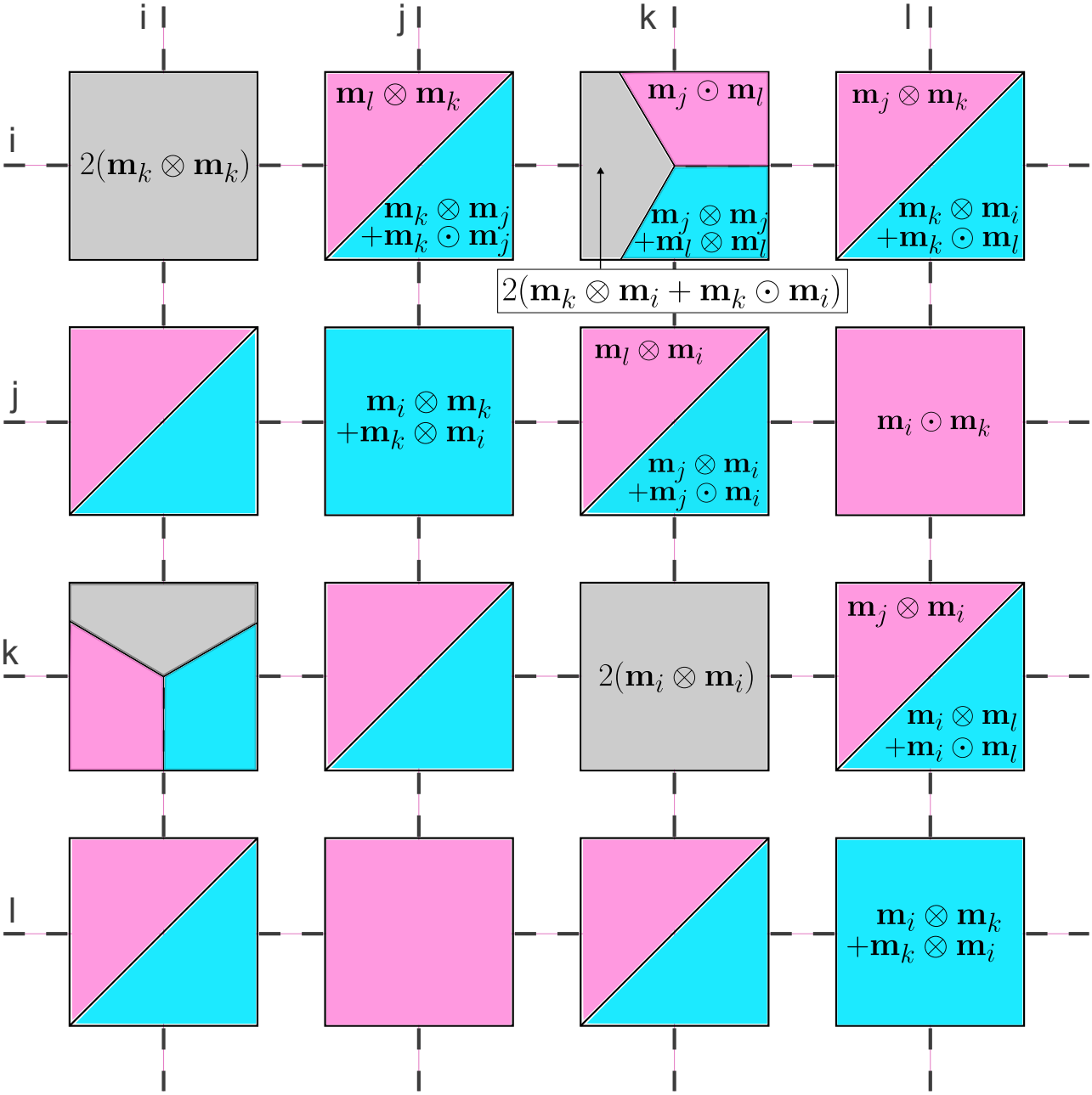


Fig. 6 | Schematic adjacency pattern for sub-matrix of the Hessian including HOI. Schematic adjacency pattern for sub-matrix of the Hessian for four magnetic moments ($\mathbf{m}_i$, $\mathbf{m}_j$, $\mathbf{m}_k$, $\mathbf{m}_l$) in nearest neighbor distance of each other (see Fig. 1a). Each block ij corresponds to the 3×3 cartesian components of the second derivatives of the energy in Eq. (1) with respect to the magnetic moments. The block colors refer to the specific HOI term contributing (biquadratic (gray), 3-site (cyan) and 4-site (pink)) HOI.

The Pairfinder algorithm explained above provides the necessary adjacency information used in the calculation of derivatives of the HOI energy with respect to the components of the magnetic moments —gradient and the matrix of second-order derivatives (Eqs. (16), (25)). On the one hand, the implementations are verified through comparing the results with analytical solutions, e.g. comparing the energy of magnetic structures with literature[80]. On the other hand, the consistency between the energy calculation and derivation of the first- and second-order derivatives with respect to the magnetization is checked via Euler's theorem for homogeneous functions. The fourth-order HOI term is a homogeneous function with order four of $3N$ variables m_i^α for $i = 1, \ldots, N$ and $\alpha \in \{x, y, z\}$:

$$E_{4-\text{spin}}(s\mathbf{m}_1, \ldots, s\mathbf{m}_N) = s^4 E_{4-\text{spin}}(\mathbf{m}_1, \ldots, \mathbf{m}_N) \tag{26}$$

with $s \neq 0$. Differentiating both sides of this equation with respect to s and taking the limit of the results with $s \to 1$ yields:

$$4E_{4-\text{spin}} = \sum_i \mathbf{m}_i \cdot (\nabla_i E_{4-\text{spin}}) \,. \tag{27}$$

Therefore the energy is expressed in terms of the gradient. Similarly, the energy can be restored from the matrix of second derivatives via

$$12E_{4-\text{spin}} = \sum_{ij} \mathbf{m}_i^T \cdot (\nabla_{ij} E_{4-\text{spin}}) \cdot \mathbf{m}_j \,. \tag{28}$$

Figure 7 c shows the energy difference of the left sides of Eqs. (27) and (28) computed with the HOI energy routine and the respective right sides, computed using the gradient and second-order derivative routines,

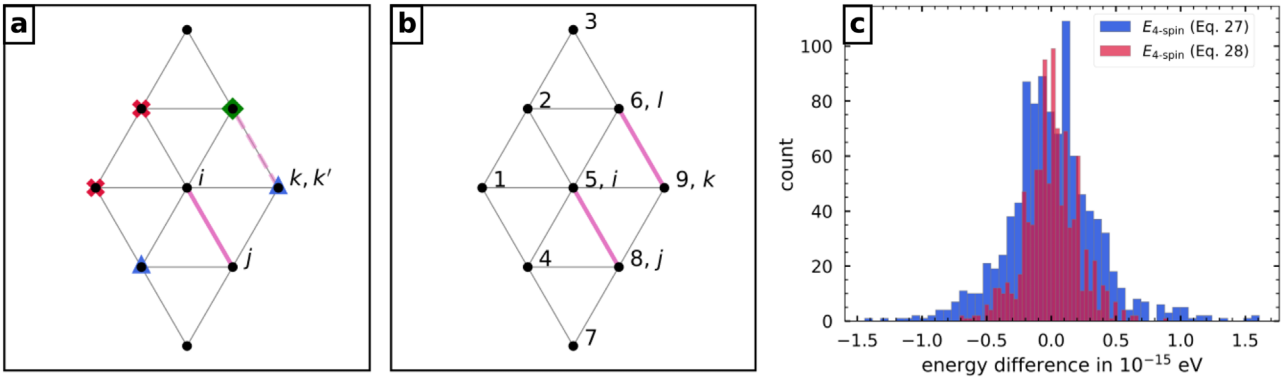


Fig. 7 | Pairfinder illustrations and energy derivative consistency test. a, b Schematic illustration of the Pairfinder algorithm utilized to calculate the neighbor relations for a specific HOI term for a 3 by 3 segment of the hexagonal lattice. Exemplary the derivation of the 4-site HOI term is shown. The moments i and j participate in the first scalar product and k, l in the latter. The sites marked by blue triangles satisfy the adjacency to i and j during the generation of the neighbor k, k'. For k, k' on the right only the site marked by the green diamond satisfies the adjacency of the fourth moment l to the others. **b** The final set of four moments with pink lines as the scalar products is illustrated in addition to the indices of the atomic sites. **c** Histogram of via Euler's theorem numerically calculated 4-spin energy differences within the atomistic spin simulation code SPINAKER. The difference between the energy and the energy via the gradient in Eq. (27) (red) and the energy via the matrix of second-order derivatives in Eq. (28) (blue) of 1000 states with random magnetization is compared.

respectively. The fluctuations are on the order of machine precision. The histogram for errors in the computation via the Hessian shows a broader distribution of numerical fluctuations, due to a quadratically increased amount of floating point operations.

Algorithm 1. Pairfinder

// declare i as the central atomic site
// reset the set-counter for the specific HOI term
$N \leftarrow 0$
// iterates the neighbors j of i
for j in neighbors(d_{ij}) **do**
  // store the index shift between i and j
  $n_{ij} \leftarrow$ indexshift(d_{ij}, j)
  for k in neighbors(d_{ik}) **do**
  $n_{ik} \leftarrow$ indexshift(d_{ik}, k)
  for k' in neighbors(d_{jk}) **do**
  $n_{jk'} \leftarrow$ indexshift(d_{jk}, k')
  if $n_{ij} + n_{jk'} - n_{ik} \neq 0$ **then**
  cycle
  end if
  // now $k = k'$, proceed with l, l' and l''
  for l in neighbors(d_{il}) **do**
  $n_{il} \leftarrow$ indexshift(d_{il}, l)
  for l' in neighbors(d_{jl}) **do**
  $n_{jl'} \leftarrow$ indexshift(d_{jl}, l')
  if $n_{ij} + n_{jl'} - n_{il} \neq 0$ **then**
  cycle
  end if
  for l'' in neighbors(d_{kl}) **do**
  $n_{kl''} \leftarrow$ indexshift(d_{kl}, l'')
  if $n_{ik} + n_{kl''} - n_{il} \neq 0$ **then**
  cycle
  end if
  // set of 4 moments found
  $N \leftarrow N + 1$
  // store index shifts
  n[N] $\leftarrow [n_{ij}, n_{ik}, n_{il}, n_{jk}, n_{jl}, n_{kl}]$
  end for
  end for
  end for
  end for
  end for
end for

Data availability

The data presented in this paper are available from the authors upon reasonable request.

Code availability

The atomistic spin simulation code is available from the authors upon reasonable request.

Received: 7 November 2025; Accepted: 2 March 2026;
Published online: 23 March 2026

References

1. Bogdanov, A. N. & Yablonskii, D. Thermodynamically stable "vortices" in magnetically ordered crystals. the mixed state of magnets. *Zh. Eksp. Teor. Fiz.* **95**, 178 (1989).
2. Nayak, A. K. et al. Magnetic antiskyrmions above room temperature in tetragonal heusler materials. *Nature* **548**, 561–566 (2017).
3. Nagaosa, N. & Tokura, Y. Topological properties and dynamics of magnetic skyrmions. *Nat. Nanotechnol.* **8**, 899–911 (2013).
4. Iwasaki, J., Mochizuki, M. & Nagaosa, N. Universal current-velocity relation of skyrmion motion in chiral magnets. *Nat. Commun.* **4**, 1463 (2013).
5. Sampaio, J., Cros, V., Rohart, S., Thiaville, A. & Fert, A. Nucleation, stability and current-induced motion of isolated magnetic skyrmions in nanostructures. *Nat. Nanotechnol.* **8**, 839–844 (2013).
6. Zhou, Y. & Ezawa, M. A reversible conversion between a skyrmion and a domain-wall pair in a junction geometry. *Nat. Commun.* **5**, 4652 (2014).
7. Woo, S. et al. Observation of room-temperature magnetic skyrmions and their current-driven dynamics in ultrathin metallic ferromagnets. *Nat. Mater.* **15**, 501–506 (2016).
8. Fert, A., Reyren, N. & Cros, V. Magnetic skyrmions: advances in physics and potential applications. *Nat. Rev. Mater.* **2**, 17031 (2017).
9. Fert, A., Cros, V. & Sampaio, J. Skyrmions on the track. *Nat. Nanotechnol.* **8**, 152–156 (2013).
10. Pinna, D. et al. Skyrmion gas manipulation for probabilistic computing. *Phys. Rev. Appl.* **9**, 064018 (2018).
11. Song, K. M. et al. Skyrmion-based artificial synapses for neuromorphic computing. *Nat. Electron.* **3**, 148–155 (2020).
12. Grollier, J. et al. Neuromorphic spintronics. *Nat. Electron.* **3**, 360–370 (2020).
13. Mühlbauer, S. et al. Skyrmion lattice in a chiral magnet. *Science* **323**, 915–919 (2009).

14. Yu, X. Z. et al. Real-space observation of a two-dimensional skyrmion crystal. *Nature* **465**, 901–904 (2010).
15. Heinze, S. et al. Spontaneous atomic-scale magnetic skyrmion lattice in two dimensions. *Nat. Phys.* **7**, 713–718 (2011).
16. Romming, N. et al. Writing and deleting single magnetic skyrmions. *Science* **341**, 636–639 (2013).
17. Meyer, S. et al. Isolated zero field sub-10 nm skyrmions in ultrathin Co films. *Nat. Commun.* **10**, 3823 (2019).
18. Muckel, F. et al. Experimental identification of two distinct skyrmion collapse mechanisms. *Nat. Phys.* **17**, 395–402 (2021).
19. Moreau-Luchaire, C. et al. Additive interfacial chiral interaction in multilayers for stabilization of small individual skyrmions at room temperature. *Nat. Nanotechnol.* **11**, 444–448 (2016).
20. Boulle, O. et al. Room-temperature chiral magnetic skyrmions in ultrathin magnetic nanostructures. *Nat. Nanotechnol.* **11**, 449–454 (2016).
21. Soumyanarayanan, A. et al. Tunable room-temperature magnetic skyrmions in Ir/Fe/Co/Pt multilayers. *Nat. Mater.* **16**, 898–904 (2017).
22. Han, M.-G. et al. Topological magnetic-spin textures in two-dimensional van der Waals $Cr_2Ge_2Te_6$. *Nano Lett.* **19**, 7859–7865 (2019).
23. Ding, B. et al. Observation of magnetic skyrmion bubbles in a van der Waals ferromagnet Fe_3GeTe_2. *Nano Lett.* **20**, 868–873 (2020).
24. Wu, Y. et al. Néel-type skyrmion in WTe_2/Fe_3GeTe_2 van der Waals heterostructure. *Nat. Commun.* **11**, 3860 (2020).
25. Yang, M. et al. Creation of skyrmions in van der Waals ferromagnet Fe_3GeTe_2 on $(Co/Pd)_n$ superlattice. *Sci. Adv.* **6**, eabb5157 (2020).
26. Wu, Y. et al. A van der Waals interface hosting two groups of magnetic skyrmions. *Adv. Mater.* **34**, 2110583 (2022).
27. Liu, C. et al. Magnetic skyrmions above room temperature in a van der Waals ferromagnet Fe_3GaTe_2. *Adv. Mater.* **36**, 2311022 (2024).
28. Kartsev, A., Augustin, M., Evans, R. F. L., Novoselov, K. S. & Santos, E. J. G. Biquadratic exchange interactions in two-dimensional magnets. *npj Computational Mater.* **6**, 150 (2020).
29. Ni, J. Y. et al. Giant biquadratic exchange in 2D magnets and its role in stabilizing ferromagnetism of $NiCl_2$ monolayers. *Phys. Rev. Lett.* **127**, 247204 (2021).
30. Xu, C. et al. Assembling diverse skyrmionic phases in Fe_3GeTe_2 monolayers. *Adv. Mater.* **34**, 2107779 (2022).
31. Li, P., Yu, D., Liang, J., Ga, Y. & Yang, H. Topological spin textures in 1*T*-phase Janus magnets: Interplay between Dzyaloshinskii-Moriya interaction, magnetic frustration, and isotropic higher-order interactions. *Phys. Rev. B* **107**, 054408 (2023).
32. Dzyaloshinskii, I. et al. Thermodynamic theory of weak ferromagnetism in antiferromagnetic substances. *Sov. Phys. JETP* **5**, 1259–1272 (1957).
33. Moriya, T. New mechanism of anisotropic superexchange interaction. *Phys. Rev. Lett.* **4**, 228–230 (1960).
34. Bode, M. et al. Chiral magnetic order at surfaces driven by inversion asymmetry. *Nature* **447**, 190–193 (2007).
35. Leonov, A. O. & Mostovoy, M. Multiply periodic states and isolated skyrmions in an anisotropic frustrated magnet. *Nat. Commun.* **6**, 8275 (2015).
36. Lin, S.-Z. & Hayami, S. Ginzburg-Landau theory for skyrmions in inversion-symmetric magnets with competing interactions. *Phys. Rev. B* **93**, 064430 (2016).
37. von Malottki, S., Dupé, B., Bessarab, P. F., Delin, A. & Heinze, S. Enhanced skyrmion stability due to exchange frustration. *Sci. Rep.* **7**, 12299 (2017).
38. Zhang, X. et al. Skyrmion dynamics in a frustrated ferromagnetic film and current-induced helicity locking-unlocking transition. *Nat. Commun.* **8**, 1717 (2017).
39. Desplat, L., Kim, J.-V. & Stamps, R. L. Paths to annihilation of first- and second-order (anti)skyrmions via (anti)meron nucleation on the frustrated square lattice. *Phys. Rev. B* **99**, 174409 (2019).
40. Goerzen, M. A., von Malottki, S., Meyer, S., Bessarab, P. F. & Heinze, S. Lifetime of coexisting sub-10 nm zero-field skyrmions and antiskyrmions. *npj Quantum Mater.* **8**, 54 (2023).
41. Paul, S., Haldar, S., von Malottki, S. & Heinze, S. Role of higher-order exchange interactions for skyrmion stability. *Nat. Commun.* **11**, 4756 (2020).
42. Kurz, P., Bihlmayer, G., Hirai, K. & Blügel, S. Three-dimensional spin structure on a two-dimensional lattice: Mn/Cu(111). *Phys. Rev. Lett.* **86**, 1106–1109 (2001).
43. Köbler, U. et al. Biquadratic exchange interactions in the europium monochalcogenides. *Z. f.ür. Phys. B Condens. Matter* **100**, 497–506 (1996).
44. Köbler, U. et al. On the failure of the bloch-kubo-dyson spin wave theory. *J. Phys. Soc. Jpn.* **70**, 3089–3097 (2001).
45. Mryasov, O. N., Freeman, A. J. & Liechtenstein, A. I. Theory of non-Heisenberg exchange: Results for localized and itinerant magnets. *J. Appl. Phys.* **79**, 4805–4807 (1996).
46. Lounis, S. & Dederichs, P. H. Mapping the magnetic exchange interactions from first principles: Anisotropy anomaly and application to Fe, Ni, and Co. *Phys. Rev. B* **82**, 180404 (2010).
47. Yoshida, Y. et al. Conical spin-spiral state in an ultrathin film driven by higher-order spin interactions. *Phys. Rev. Lett.* **108**, 087205 (2012).
48. Krönlein, A. et al. Magnetic Ground State Stabilized by Three-Site Interactions: Fe/Rh(111). *Phys. Rev. Lett.* **120**, 207202 (2018).
49. Romming, N. et al. Competition of Dzyaloshinskii-Moriya and Higher-Order Exchange Interactions in Rh/Fe Atomic Bilayers on Ir(111). *Phys. Rev. Lett.* **120**, 207201 (2018).
50. Spethmann, J. et al. Discovery of magnetic single- and triple-**q** states in $Mn/Re(0001)$. *Phys. Rev. Lett.* **124**, 227203 (2020).
51. Gutzeit, M. et al. Nano-scale collinear multi-q states driven by higher-order interactions. *Nat. Commun.* **13**, 5764 (2022).
52. Takahashi, M. Half-filled Hubbard model at low temperature. *J. Phys. C: Solid State Phys.* **10**, 1289 (1977).
53. MacDonald, A. H., Girvin, S. M. & Yoshioka, D. $\frac{t}{U}$ expansion for the Hubbard model. *Phys. Rev. B* **37**, 9753–9756 (1988).
54. Hoffmann, M. & Blügel, S. Systematic derivation of realistic spin models for beyond-Heisenberg solids. *Phys. Rev. B* **101**, 024418 (2020).
55. von Malottki, S., Bessarab, P. F., Haldar, S., Delin, A. & Heinze, S. Skyrmion lifetime in ultrathin films. *Phys. Rev. B* **99**, 060409 (2019).
56. Varentcova, A. S. et al. Toward room-temperature nanoscale skyrmions in ultrathin films. *npj Comput. Mater.* **6**, 193 (2020).
57. Goerzen, M. A. *Thermal equilibrium and stability of complementary topological solitons in two-dimensional magnets*. Ph.D. thesis, University of Kiel (2024).
58. Hagemeister, J., Romming, N., von Bergmann, K., Vedmedenko, E. Y. & Wiesendanger, R. Stability of single skyrmionic bits. *Nat. Commun.* **6**, 8455 (2015).
59. Wild, J. et al. Entropy-limited topological protection of skyrmions. *Sci. Adv.* **3**, e1701704 (2017).
60. Desplat, L., Suess, D., Kim, J.-V. & Stamps, R. L. Thermal stability of metastable magnetic skyrmions: Entropic narrowing and significance of internal eigenmodes. *Phys. Rev. B* **98**, 134407 (2018).
61. Haldar, S., von Malottki, S., Meyer, S., Bessarab, P. F. & Heinze, S. First-principles prediction of sub-10-nm skyrmions in Pd/Fe bilayers on Rh(111). *Phys. Rev. B* **98**, 060413 (2018).
62. Beyer, B. et al. Bilayer triple-q state driven by interlayer higher-order exchange interactions. *Phys. Rev. B* **112**, 094430 (2025).
63. Dupé, B., Hoffmann, M., Paillard, C. & Heinze, S. Tailoring magnetic skyrmions in ultra-thin transition metal films. *Nat. Commun.* **5**, 4030 (2014).
64. Arya, M. et al. A new skyrmion topological transition driven by higher-order exchange interactions in Janus MnSeTe. *Nano Lett.* **25**, 16703 (2025).
65. von Malottki, S., Goerzen, M. A., Schrautzer, H., Bessarab, P. F. & Heinze, S. Eigenmode following for direct entropy calculation and characterization of magnetic systems. *arXiv:2503.12109* (2025).

66. Bocdanov, A. & Hubert, A. The properties of isolated magnetic vortices. *Phys. status solidi (b)* **186**, 527–543 (1994).
67. Schrautzer, H., Sallermann, M., Bessarab, P. F. & Jónsson, H. Identification of mechanisms of magnetic transitions using an efficient method for converging on first-order saddle points. *Phys. Rev. B* **112**, 104433 (2025).
68. Müller, G. P. et al. Duplication, collapse, and escape of magnetic skyrmions revealed using a systematic saddle point search method. *Phys. Rev. Lett.* **121**, 197202 (2018).
69. Bessarab, P. F. et al. Lifetime of racetrack skyrmions. *Sci. Rep.* **8**, 3433 (2018).
70. Bessarab, P. F., Uzdin, V. M. & Jónsson, H. Harmonic transition-state theory of thermal spin transitions. *Phys. Rev. B* **85**, 184409 (2012).
71. Schrautzer, H., von Malottki, S., Bessarab, P. F. & Heinze, S. Effects of interlayer exchange on collapse mechanisms and stability of magnetic skyrmions. *Phys. Rev. B* **105**, 014414 (2022).
72. Gutzeit, M., Haldar, S., Meyer, S. & Heinze, S. Trends of higher-order exchange interactions in transition metal trilayers. *Phys. Rev. B* **104**, 024420 (2021).
73. Reichhardt, C., Reichhardt, C. J. O. & Milošević, M. V. Statics and dynamics of skyrmions interacting with disorder and nanostructures. *Rev. Mod. Phys.* **94**, 035005 (2022).
74. Arjana, I. G., Lima Fernandes, I., Chico, J. & Lounis, S. Sub-nanoscale atom-by-atom crafting of skyrmion-defect interaction profiles. *Sci. Rep.* **10**, 14655 (2020).
75. Mellado, P. Magnetic moiré systems: a review. *J. Phys.: Condens. Matter* **37**, 323001 (2025).
76. Amirabbasi, M. & Kratzer, P. Effect of biquadratic magnetic exchange interaction in the 2d antiferromagnets $m\mathrm{ps}_3$ (m = Mn, Fe, Co, Ni). *Phys. Rev. Mater.* **8**, 084005 (2024).
77. Hohenberg, P. & Kohn, W. Inhomogeneous electron gas. *Phys. Rev.* **136**, B864–B871 (1964).
78. Kohn, W. & Sham, L. J. Self-consistent equations including exchange and correlation effects. *Phys. Rev.* **140**, A1133–A1138 (1965).
79. Bessarab, P. F., Uzdin, V. M. & Jónsson, H. Method for finding mechanism and activation energy of magnetic transitions, applied to skyrmion and antivortex annihilation. *Computer Phys. Commun.* **196**, 335–347 (2015).
80. Kurz, P.*Non-Collinear Magnetism at Surfaces and in Ultrathin Films*. Ph.D. thesis, Rheinisch-Westfälische Technische Hochschule Aachen (2000).

Acknowledgements

H.S. acknowledges financial support from the Icelandic Research Fund (grant No. 239435). P.F.B. acknowledges financial support from the Icelandic Research Fund (Grants No. 2410333 and No. 217750), the University of Iceland Research Fund (Grant No. 15673), the Swedish Research Council (Grant No. 2020-05110), and the Crafoord Foundation (Grant No. 20231063). S. Ha and S. He. gratefully acknowledge financial support from the Deutsche Forschungsgemeinschaft (DFG, German Research Foundation) through SPP2137 “Skyrmionics” (project no. 462602351) and project no. 418425860.This work was performed using HPC resources available at the Kiel University Computing Centre. H.S. thanks S. Paul and S. von Malottki for valuable discussions and M.A.G. thanks T. Drevelow for valuable discussions.

Author contributions

H.S. performed the calculations and prepared the figures. H.S., P.F.B. and S. He. analyzed the data. B.B. implemented and tested higher-order interactions in the code supported by M.A.G., H.S. and S. Ha. All authors discussed the results. H.S. and M.A.G. wrote the first version of the manuscript, and all authors contributed to the final version.

Funding

Open Access funding enabled and organized by Projekt DEAL.

Competing interests

The authors declare no competing interests.

Additional information

Supplementary information The online version contains supplementary material available at https://doi.org/10.1038/s41524-026-02034-9.

Correspondence and requests for materials should be addressed to Stefan Heinze.

Reprints and permissions information is available at http://www.nature.com/reprints

Publisher’s note Springer Nature remains neutral with regard to jurisdictional claims in published maps and institutional affiliations.

Open Access This article is licensed under a Creative Commons Attribution 4.0 International License, which permits use, sharing, adaptation, distribution and reproduction in any medium or format, as long as you give appropriate credit to the original author(s) and the source, provide a link to the Creative Commons licence, and indicate if changes were made. The images or other third party material in this article are included in the article’s Creative Commons licence, unless indicated otherwise in a credit line to the material. If material is not included in the article’s Creative Commons licence and your intended use is not permitted by statutory regulation or exceeds the permitted use, you will need to obtain permission directly from the copyright holder. To view a copy of this licence, visit http://creativecommons.org/licenses/by/4.0/.

© The Author(s) 2026